iScience

CellPress
OPEN ACCESS

Article

Impaired formation of high-order gephyrin oligomers underlies gephyrin dysfunction-associated pathologies

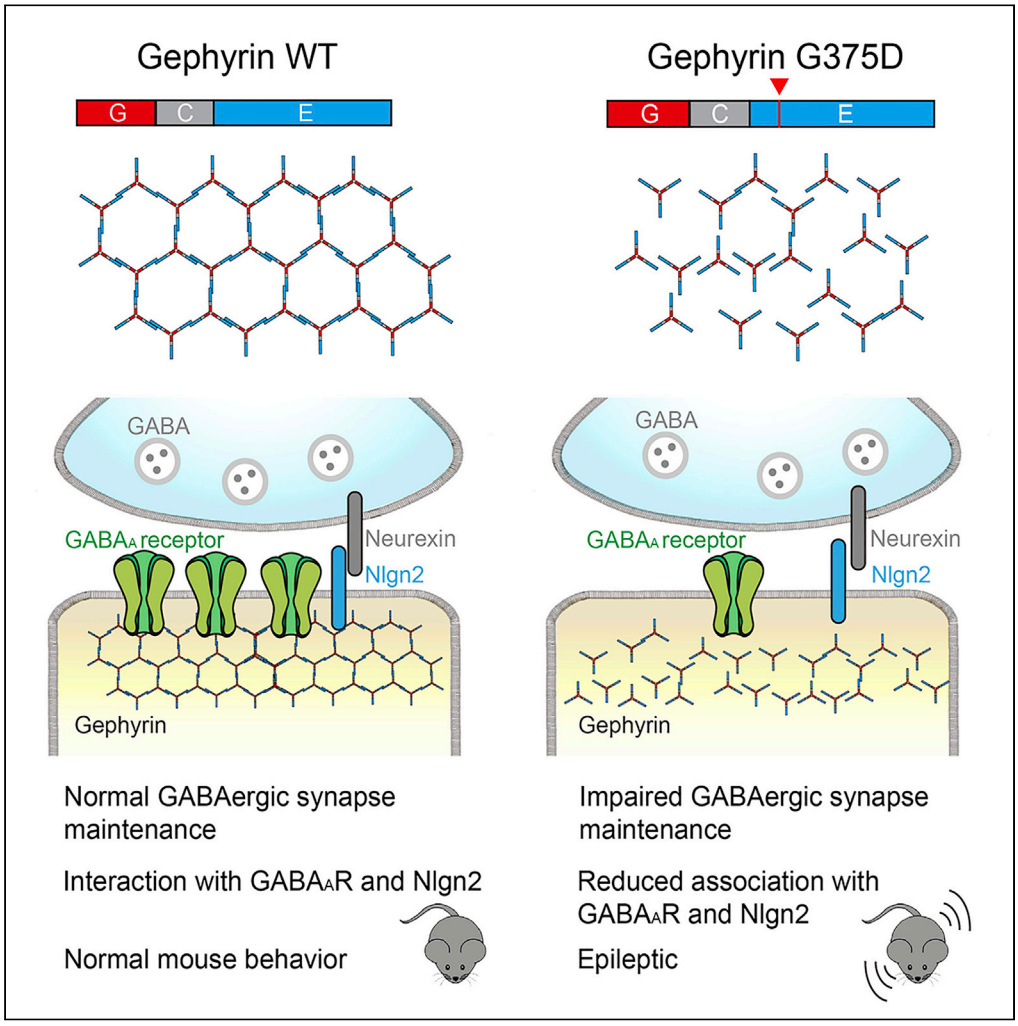

Seungjoon Kim, Mooseok Kang, Dongseok Park, ..., Jaewon Ko, Iksoo Chang, Ji Won Um

iksoochang@dgist.ac.kr (I.C.)
jiwonum@dgist.ac.kr (J.W.U.)

HIGHLIGHTS

Gephyrin G375D reduces the formation of E-domain-mediated gephyrin oligomers

Gephyrin G375D impairs GABAergic synapse maintenance *in vivo*

Gephyrin G375D increases susceptibility to kainic acid-induced seizures *in vivo*

Gephyrin G375D displays reduced interactions with $GABA_A$ receptors and Nlgn2 *in vivo*

Kim et al., iScience *24*, 102037
February 19, 2021 © 2021 The Author(s).
https://doi.org/10.1016/j.isci.2021.102037

iScience

CellPress
OPEN ACCESS

Article

Impaired formation of high-order gephyrin oligomers underlies gephyrin dysfunction-associated pathologies

Seungjoon Kim,[1,6] Mooseok Kang,[1,2,6] Dongseok Park,[1] Ae-Ree Lee,[1,2] Heinrich Betz,[3] Jaewon Ko,[1,5] Iksoo Chang,[1,2,4,5,*] and Ji Won Um[1,2,5,7,*]

SUMMARY

Gephyrin is critical for the structure, function, and plasticity of inhibitory synapses. Gephyrin mutations have been linked to various neurological disorders; however, systematic analyses of the functional consequences of these mutations are lacking. Here, we performed molecular dynamics simulations of gephyrin to predict how six reported point mutations might change the structural stability and/or function of gephyrin. Additional *in silico* analyses revealed that the A91T and G375D mutations reduce the binding free energy of gephyrin oligomer formation. Gephyrin A91T and G375D displayed altered clustering patterns in COS-7 cells and nullified the inhibitory synapse-promoting effect of gephyrin in cultured neurons. However, only the G375D mutation reduced gephyrin interaction with $GABA_A$ receptors and neuroligin-2 in mouse brain; it also failed to normalize deficits in GABAergic synapse maintenance and neuronal hyperactivity observed in hippocampal dentate gyrus-specific gephyrin-deficient mice. Our results provide insights into biochemical, cell-biological, and network-activity effects of the pathogenic G375D mutation.

INTRODUCTION

Recent research in sequencing and genomics has shown clear associations of numerous synaptic genes with a variety of neuropsychiatric and neurodevelopmental diseases, including autism spectrum disorders (ASDs), schizophrenia and epilepsy, giving rise to the 'synaptopathy' concept (Medland et al., 2014; Sestan and State, 2018; State and Levitt, 2011). However, in addition to the complex inheritance pattern of the culprit synaptic genes implicated in these disorders, complexities in genetic causation profiles have challenged our ability to establish how dysfunction(s) of risk gene-encoded proteins at synapses precisely contribute to disease onset and/or progression (Heinzen et al., 2015). In cases of highly variable point mutants, empirical approaches combined with *in silico* analyses can be used *a priori* to investigate whether these mutations are loss- or gain-of-function mutations and to determine how altered properties might affect specific aspects of synapse development and animal behavior [e.g. (Anastasia et al., 2013; Bath and Lee, 2006; Falivelli et al., 2012; Kang et al., 2016; Riccardi et al., 2019; Südhof, 2017)].

Gephyrin contributes to the accumulation of $GABA_A$ receptors at postsynaptic sites by interacting with several key GABAergic synapse-specific proteins, enabling efficient inhibitory synaptic transmission (Betz, 1998; Choii and Ko, 2015; Fritschy et al., 2008; Groeneweg et al., 2018; Pizzarelli et al., 2019; Tyagarajan and Fritschy, 2014). In addition, gephyrin is known to be required for synaptic clustering of glycine receptors (GlyRs) in the spinal cord and for molybdoenzyme activity in non-neuronal tissues (Feng et al., 1998; Kirsch et al., 1993; Stallmeyer et al., 1999). Gephyrin is composed of three functional domains: an N-terminal G-domain, a central C-domain, and a C-terminal E-domain (Choii and Ko, 2015; Kim et al., 2006; Pizzarelli et al., 2019; Sola et al., 2004). At postsynaptic sites, gephyrin assembles through G- and E-domain–mediated interactions into a complex submembranous lattice that is dynamically regulated by a number of posttranslational modifications and interactions with other binding proteins (Choii and Ko, 2015; Groeneweg et al., 2018; Tyagarajan and Fritschy, 2014). The lattice formed by gephyrin is multimeric (Saiyed et al., 2007), with the G-domain-mediated trimeric form being prominent in bacteria (Sander et al., 2013). Trimerization of G-domains and dimerization of E-domains are considered essential for the ability of gephyrin to form hexagonal membrane-associated scaffolds and recruit GlyRs and $GABA_A$ receptors

[1]Department of Brain and Cognitive Sciences, Daegu Gyeongbuk Institute of Science and Technology (DGIST), Daegu 42988, Korea

[2]Core Protein Resources Center, DGIST, Daegu 42988, Korea

[3]Max Planck Institute for Medical Research, Jahnstrasse 29, 69120 Heidelberg, Germany

[4]Supercomputing Bigdata Center, DGIST, Daegu 42988, Korea

[5]Senior authors

[6]These authors contributed equally

[7]Lead contact

*Correspondence: iksoochang@dgist.ac.kr (I.C.), jiwonum@dgist.ac.kr (J.W.U.)

https://doi.org/10.1016/j.isci.2021.102037

This is an open access article under the CC BY license (http://creativecommons.org/licenses/by/4.0/).

($GABA_ARs$) to developing synapses (Calamai et al., 2009; Kneussel and Betz, 2000; Saiyed et al., 2007; Sola et al., 2004). Not surprisingly, gephyrin has been implicated in various brain disorders, including autism, schizophrenia, Alzheimer's disease, and epilepsy (Agarwal et al., 2008; Dejanovic et al., 2014; Forstera et al., 2010; Kiss et al., 2016; Lionel et al., 2013). Sequencing studies have suggested that irregular alternative splicing within the G-domain coding region, large exonic deletions, and missense mutations are linked to neuronal or metabolic dysfunction of gephyrin (Dejanovic et al., 2014, 2015; Forstera et al., 2010; Lionel et al., 2013). However, whether the resulting changes in gephyrin structure directly affect the formation of intact hexagonal multimeric lattices or are linked to GABAergic synapse development has not been investigated. A heterozygous missense mutation, p.Gly375Asp (G375D) in the gephyrin gene, *GPHN*, has been reported to disrupt the function of endogenous gephyrin proteins in neurons, resulting in reduced binding affinity for $GABA_ARs$ and GlyRs as well as impaired molybdenum cofactor synthesis activity (Dejanovic et al., 2015). However, apart from these phenomenological descriptions of gephyrin mutations based on a set of functional assays, little is understood about whether and how the reported mutations actually alter gephyrin's oligomerization properties and interactions with other synaptic proteins to contribute to changes in gephyrin scaffold formation.

In the present study, we performed atomic-scale molecular dynamics (MD) simulations combined with thermodynamic integration (TI) calculations for wild-type (WT) gephyrin and a subset of gephyrin missense mutants associated with ASDs or epileptic encephalopathy, to test the hypothesis that these mutations affect the structural stability of the multimeric gephyrin complex. The gephyrin mutants, A91T and G375D, which displayed altered binding free energies *in silico*, were chosen for further functional analyses. Remarkably, only G375D, and not A91T, exerted loss-of-function phenotypes *in vivo*, including an abnormally heightened epileptogenic potential. Our study provides insights into gephyrin dysfunction-associated synaptopathies and underscores the potential of supercomputing-based simulations to predict deleterious effects of synaptic protein mutations.

RESULTS

Molecular dynamics simulation-based prediction of conformational changes produced by gephyrin missense mutations associated with neurological disorders

Six missense mutations of gephyrin—V43L, A91T, G375D, G578A, G578S, and D697N—have previously been linked to ASDs and/or epileptic encephalopathy (Dejanovic et al., 2015; Lionel et al., 2013). Among these, gephyrin G375D has been shown to disrupt neuronal and metabolic functions of gephyrin (Dejanovic et al., 2015). Specifically, G375D acts in a dominant-negative manner to inhibit complex formation between gephyrin and $GABA_ARs$ or GlyRs, and further compromises molybdenum cofactor synthesis activity (Dejanovic et al., 2015). Although gephyrin G375D was demonstrated to form oligomers with gephyrin WT by size-exclusion chromatography, it has not been clarified whether this mutation impairs formation of gephyrin multimers by severing the structure of the E-domain, where the G375 residue is located.

To address whether pathogenic gephyrin mutations located in G- or E-domains affect the stability of the hexagonal gephyrin scaffold, we explored potential accompanying conformational changes by performing supercomputing MD simulations of gephyrin G-domain trimers and E-domain dimers. V43, A91, G375, G578, and D697 residues in human gephyrin are conserved in rat gephyrin and correspond to V43, A91, G375, G545, and D664 residues, respectively, of rat gephyrin (Figure 1A). For structural modeling studies and functional assays, we produced the rat gephyrin G-domain (amino acids 1–188) mutants V43L and A91T and E-domain (amino acids 318–736) G375D, G545A, G545S, and D664N by replacing these conserved residues with the corresponding amino acids found in human patients (Figure 1B). The G-domain trimer has a 3-fold symmetry in which the α-helix and loops are involved in the interface between monomers (Schwarz et al., 2001; Sola et al., 2001) (Figures 1C and 1D). V43 is located on the outer α-helix of the trimer and A91 is located near the binding interface with other chains (Figure 1D). Our MD simulations of V43L and A91T mutants indicated no conformational change in the monomer or trimer. It also revealed no difference in structural fluctuations of residues during a 0.5–1 μs simulation, except for the terminal loop, and showed no structural difference between WT and mutant proteins, even near the mutated residues (Figure S1A).

The E-domain dimer has 2-fold symmetry, and each monomer consists of four subdomains, of which the receptor-binding subdomains (residues 654–736) are known to bind to $GABA_ARs$ and GlyRs (Kim et al.,

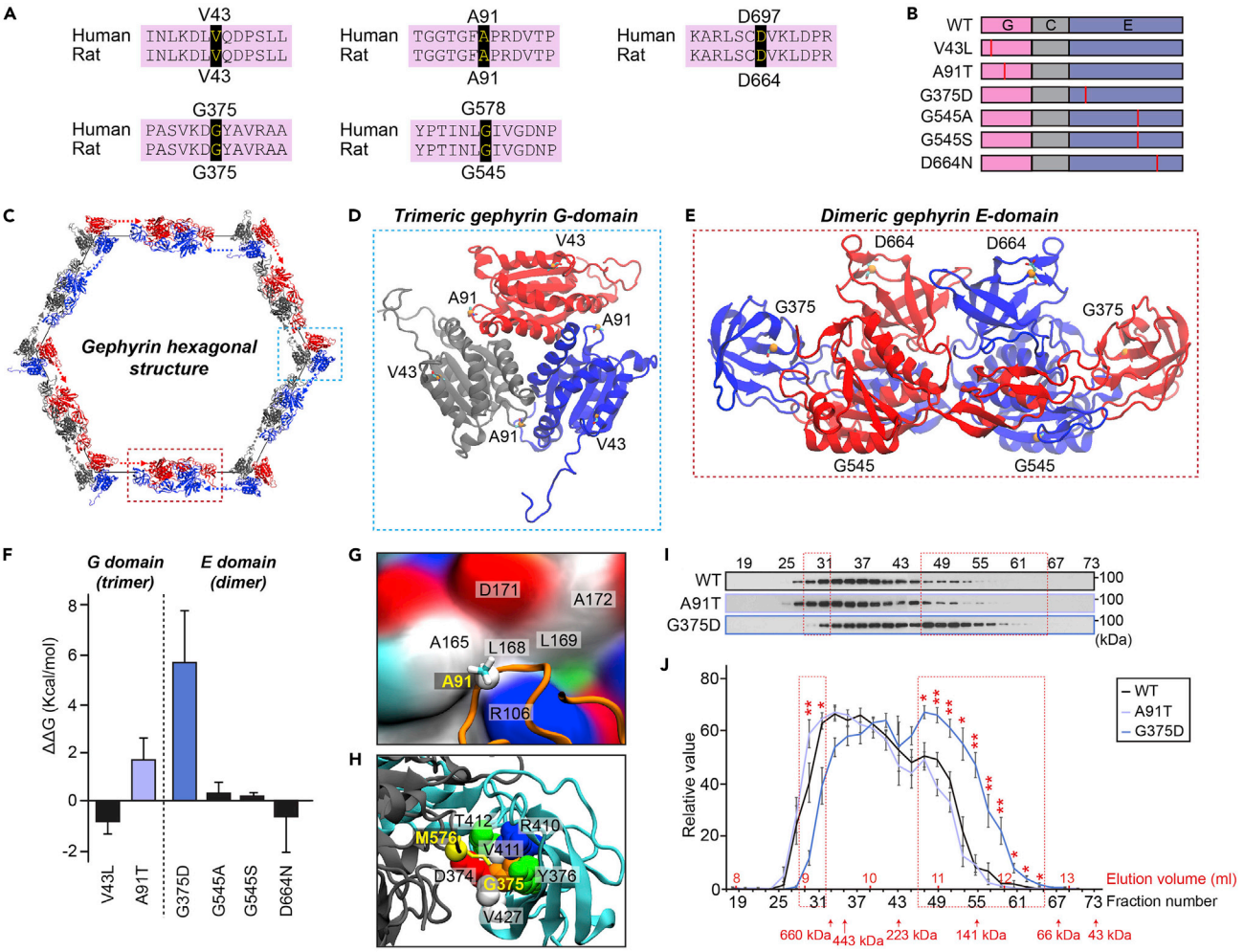

Figure 1. A human gephyrin missense mutation associated with epileptic encephalitis alters multimer binding stability

(A) Alignment and conservation between human gephyrin- and rat gephyrin residues that are mutated in human patients with epileptic encephalopathy or ASDs.

(B) Schematic diagrams of gephyrin WT and its mutants. Abbreviations: G, G-domain; C, C-domain; E, E-domain.

(C) Schematic depiction of gephyrin hexagonal lattices.

(D) Structure of G-domain trimers and position of point mutations in gephyrin.

(E) Structure of E-domain dimers and position of point mutations in gephyrin.

(F) Multimer binding free energy difference between gephyrin WT and the indicated point mutants, as calculated by thermodynamic integration analyses. Numerical values per mutation points were averaged. Data are represented as means ± SDs.

(G) A91 and hydrophobic pockets in the binding interface between gephyrin G-domains.

(H) G375 positioned inside of the β-strand bundle at the binding interface between chains. Bead and surface colors indicate the following: white, hydrophobic; green, hydrophilic; red, negatively charged; blue, positively charged; and yellow, methionine.

(I) Extracts of HEK293T cells transfected with untagged gephyrin WT or its mutants (A91T or G375D) were fractionated on a gel filtration column. Fractions were analyzed by immunoblotting using anti-gephyrin antibodies.

(J) Quantification of expression levels of gephyrin WT and its mutants (A91T or G375D) in each fraction. Data are means ± SEMs (*p < 0.05, **p < 0.01; WT versus G375D; Mann-Whitney *U* test; n = 5/group).

2006; Maric et al., 2014; Sola et al., 2004). G375 is located in the β-strand bundle subdomain (residues 367–463) on one side, D664 is located in the receptor-binding subdomain, and G545 is located on the other side (Figures 1C and 1E). MD simulations performed on gephyrin WT, G375D, G545A, G545S, and D664N mutants showed large structural fluctuations in the β-strand bundle subdomain of both WT and mutants (Figure S1B). However, this type of fluctuation was observed in all MD trajectories, regardless of mutation status, and there were no conformational changes in monomers or dimers at or near the mutation interface.

We initially expected that a single mutation could alter the structure of gephyrin or influence the trimeric and/or dimeric structure but our MD simulation results predicted no significant structural changes.

Calculation of differences in binding stability between gephyrin WT and mutants using TI MD simulations

Because single point mutations in gephyrin conferred no significant conformational changes on monomeric or multimeric structures of gephyrin (Figure S1), we next examined effects of the mutation on the binding stability of the multimer. Using TIMD simulations to calculate the binding free energy difference between WT and mutants of the G-domain trimer and E-domain dimer, we found that the binding free energies of the A91T and G375D mutants, in which the mutations occur near the binding interface, were significantly changed compared with that of the WT (Figure 1F). Specifically, the binding free energy difference of A91T relative to the WT was determined to be 5.1 $\pm$ 2.7 kcal/mol, or 1.7 kcal/mol per mutation point (Figure 1F). A91 is a hydrophobic residue located at the binding interface of the G-domain trimer, where it is exposed to the outside and bound to a hydrophobic pocket consisting of A165, L168, L169, and A172 (Figure 1G). Mutation of this alanine to the hydrophilic threonine weakens hydrophobic interaction with this pocket, reducing the binding stability of the A91T G-domain trimer compared with that of the WT. However, given thermal fluctuation effects, the binding free energy difference of A91T might be non-significant.

For G375D, the binding free energy difference relative to WT was determined to be 11.3 $\pm$ 4.3 kcal/mol, a highly significant difference of 5.7 kcal/mol per mutation point (Figure 1F). G375 is located at the center of the β-strand bundle subdomain and lies close to the binding interface of the $GABA_AR$- and GlyR-binding subdomain of another E-domain (Figure 1H). At the binding interface of the two subdomains, the hydrophobic side chain of M576 in the receptor-binding subdomain is fit into the pocket of the β-strand bundle subdomain consisting of D374, G375, Y376, R410, V411, T412, and V427. Changing this central glycine to a negatively charged aspartic acid breaks the electrostatic equilibrium and spatial conditions of the binding pocket, decreasing the binding stability of the E-domain dimer and weakening contacts of the monomers. Taken together, our MD simulations revealed that A91T and G375D mutations lower the binding affinity of the multimer rather than directly altering the entire structure, thereby affecting the stability of gephyrin hexagonal structures.

To validate these structural predictions experimentally, we performed gel filtration chromatography to test whether A91T and G375D mutations affect the abundance of gephyrin oligomers formed upon expression in HEK293T cells (Figures 1I and 1J). Immunoblot analyses of each fraction revealed the similar elution patterns for gephyrin A91T and gephyrin WT. In contrast, under the same conditions a significant fraction of gephyrin G375D was shifted to lower molecular weight positions (Figures 1I and 1J). Specifically, gephyrin G375D abundance was significantly lower than that of WT in > 600 kDa fractions (fractions 27–33) but was more abundant in < 200-kDa fractions (fractions 49–61) (Figures 1I and 1J). These results suggest that gephyrin G375D higher-order oligomers are less frequent or are less stable, than those of the WT protein, in keeping with the results of our TIMD simulations.

Gephyrin G375D is defective in promoting GABAergic synapse formation *in vitro*

To assess whether the mutations in the *GPHN* gene described above alter the clustering properties of gephyrin, we generated enhanced green fluorescence protein (EGFP)-tagged constructs of gephyrin WT and its mutants (Figure 2A). Immunoblot analyses showed that expression levels of the tagged gephyrin point mutants were comparable to those of WT (Figure 2B). Recombinant gephyrin is known to form large intracellular aggregates in non-neuronal cells (Kins et al., 2000). As previously reported, EGFP-gephyrin WT consistently formed large intracellular clusters when expressed in COS-7 cells (Figure 2C). Under the same conditions, exogenously expressed gephyrin A91T formed significantly more, but smaller, aggregates, whereas G375D produced tiny aggregates in only 30% of transfected cells (Figures 2C and 2D). The other gephyrin mutants examined, V43L, G545A, G545S, and D664N, generated aggregates similar to those formed by gephyrin WT (Figures 2C and 2D). These results are consistent with the reduced oligomerization potential of A91T and G375D, but unchanged oligomerization properties of the other mutants.

To determine whether the gephyrin mutations indicated above affect GABAergic synaptic targeting of gephyrin mutants, we transfected cultured hippocampal neurons with EGFP-tagged gephyrin WT or the indicated mutants at 10 days *in vitro* (DIV10), and immunostained transfected neurons for the

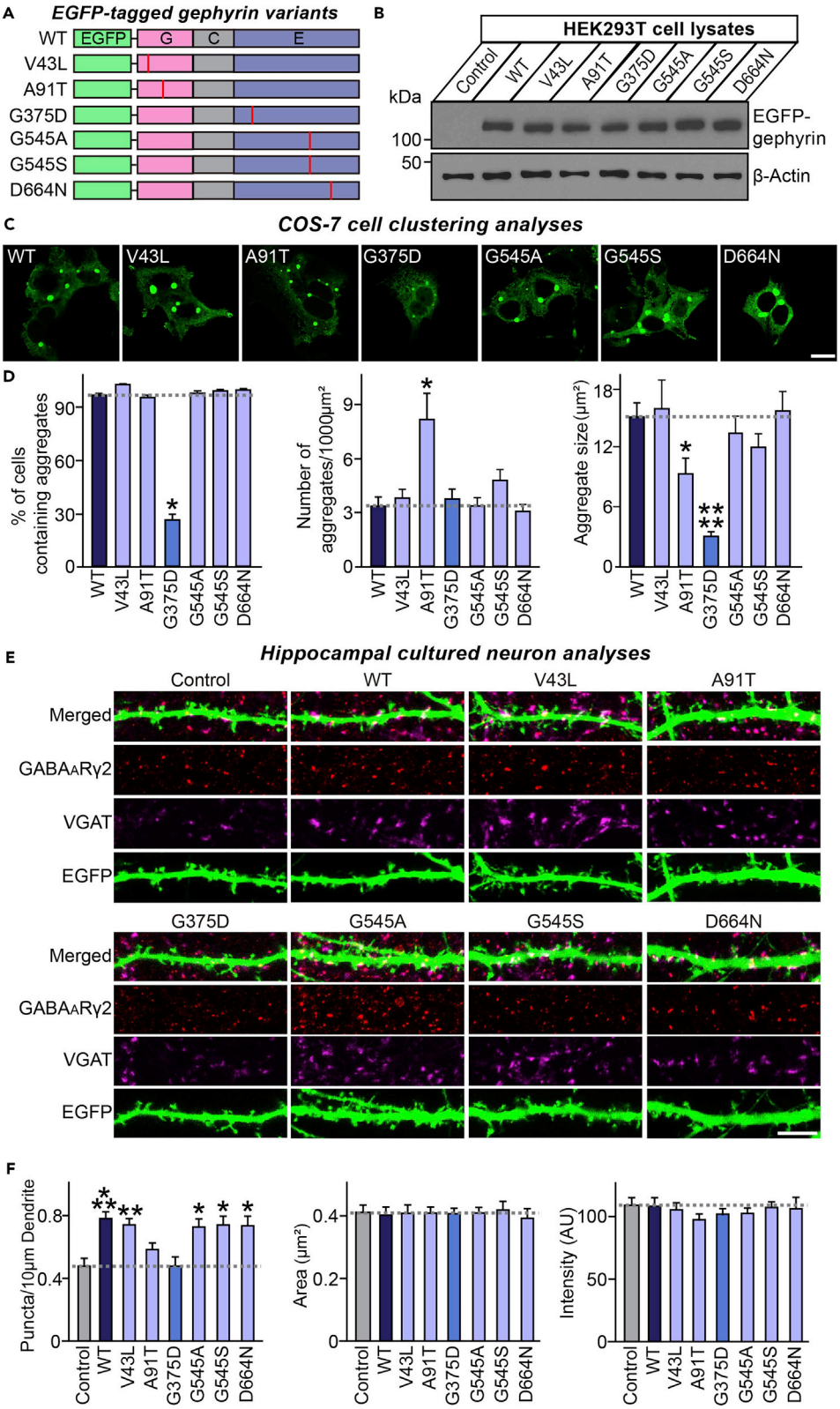
A
EGFP-tagged gephyrin variants
WT
V43L
A91T
G375D
G545A
G545S
D664N
EGFP
G
C
E
B
HEK293T cell lysates
Control
WT
V43L
A91T
G375D
G545A
G545S
D664N
kDa
100
50
EGFP-gephyrin
β-Actin
C
COS-7 cell clustering analyses
D
% of cells containing aggregates
Number of aggregates/1000μm²
Aggregate size (μm²)
E
Hippocampal cultured neuron analyses
Merged
GABAARγ2
VGAT
EGFP
F
Puncta/10μm Dendrite
Area (μm²)
Intensity (AU)

Figure 2. Gephyrin G375D, but not A91T, is defective in promoting GABAergic synapse formation in cultured hippocampal neurons

(A) Schematic diagrams of gephyrin WT and its mutants. Abbreviations: G, G-domain; C, C-domain; E, E-domain.

(B) Immunoblotting of lysates from HEK293T cells transfected with EGFP-tagged gephyrin WT or its mutants using anti-gephyrin antibodies. An anti-β-actin antibody was used as a normalization control.

(C) Representative images of COS-7 cells transfected with EGFP-gephyrin WT or its mutants. Scale bar, 10 μm (applies to all images).

(D) Quantification of the percentage of COS-7 cells with large cytoplasmic intracellular aggregates, the number of aggregates per 1000 μm^2, and average aggregate size. Data are presented as means ± SEMs from three independent experiments (*$p < 0.05$, ****$p < 0.0001$; non-parametric ANOVA with Kruskal-Wallis test followed by *post hoc* Dunn's multiple comparison test).

(E) Representative images of cultured hippocampal neurons transfected at DIV10 with EGFP alone (Control) or cotransfected with EGFP alone and EGFP-tagged gephyrin WT or its mutants, and analyzed at DIV14 by triple-immunofluorescence staining using anti-$GABA_AR\gamma2$ (red), anti-VGAT (magenta) and anti-EGFP (green) antibodies. Scale bar, 10 μm (applies to all images).

(F) Summary graphs of the effects of overexpressing gephyrin WT or its mutants on $GABA_AR\gamma2^+VGAT^+$ puncta density (left), $GABA_AR\gamma2^+VGAT^+$ puncta size (middle), and $GABA_AR\gamma2^+VGAT^+$ puncta intensity (right). Data are presented as means ± SEMs from three independent experiments (2–3 dendrites per transfected neurons were analyzed and group-averaged; *$p < 0.05$, **$p < 0.01$, ***$p < 0.001$; non-parametric ANOVA with Kruskal-Wallis test followed by *post hoc* Dunn's multiple comparison test).

GABAergic presynaptic marker, VGAT (vesicular GABA transporter), and the postsynaptic $GABA_A$ receptor γ2 subunit ($GABA_AR\gamma2$) at DIV14. An assessment of the subcellular localization of gephyrin mutants, visualized by monitoring GFP immunofluorescence, revealed that gephyrin WT was mainly distributed to GABAergic synaptic sites, whereas both A91T and G375D were diffusely distributed along dendrites of the transfected neurons, compared to gephyrin WT and other mutants (Figure S2). Next, to determine whether gephyrin mutations also compromise the ability of gephyrin to promote GABAergic synapse formation, we transfected cultured hippocampal neurons with EGFP-tagged gephyrin WT or mutants at DIV10, together with EGFP empty vector to clearly visualize the dendritic segments and immunostained transfected neurons for the GABAergic synaptic markers, VGAT and $GABA_AR\gamma2$, at DIV14. Overexpression of gephyrin WT in cultured hippocampal neurons significantly increased the density, but not the size or fluorescence intensity of $VGAT^+/GABA_AR\gamma2^+$ puncta, as compared with neurons expressing EGFP alone (Figures 2E and 2F). Notably, overexpression of the mutants, V43L, G545A, G545S, or D664N, increased $VGAT^+/GABA_AR\gamma2^+$ puncta density to a similar extent as gephyrin WT, whereas overexpression of G375D or A91T had no such effect on synaptic marker puncta (Figures 2E and 2F). Collectively, these results are consistent with the idea that the gephyrin G375D mutation impairs the formation of or destabilizes higher-order gephyrin oligomers, thereby disrupting clustering of postsynaptic $GABA_A$ receptors.

Gephyrin G375D reduces GABAergic synapse numbers in hippocampal dentate gyrus granule neurons of adult mice

To extend the observations made with the gephyrin mutants A91T and G375D to neurons *in vivo*, we used gephyrin floxed mice (O'Sullivan et al., 2016) stereotactically injected in the hippocampal dentate gyrus (DG) with adeno-associated viruses (AAVs) expressing either mCherry-fused nuclear Cre-recombinase or a non-functional mutant version of Cre-recombinase (ΔCre), as a control, to generate DG-specific gephyrin-knockout (KO) mice (Figure 3A). To determine whether the effects of gephyrin deletion in the DG on GABAergic synapse maintenance could be rescued, we also co-injected AAVs expressing Cre-recombinase with AAVs expressing EGFP-fused WT or mutant (A91T or G375D) gephyrin (Figure 3A). Targeted delivery of AAVs into the DG of mice was verified (Figures S3A and S3B), and AAV coinfection efficiency was comparable among all groups (Cre and gephyrin WT, 98.05 ± 0.70%; Cre and gephyrin A91T, 97.58 ± 0.65%; and Cre and gephyrin G375D, 97.95 ± 0.79%) (Figure S3C). Expression of Cre-recombinase and gephyrin WT or mutant proteins was validated by immunoblotting AAV-infected DG brain tissues with anti-gephyrin antibodies (Figure 3B).

We performed immunohistochemical analyses to probe whether the loss of gephyrin affects GABAergic synapse numbers in the DG (Figures 3C, 3D, S4, and S5). Quantitative immunofluorescence analyses revealed significant decreases in the puncta densities of $GABA_AR\gamma2$ and VGAT in the DG granular cell layer, molecular layer and hilus upon DG-specific Cre expression (Figures 3C, 3D, and S5). This is consistent with the interpretation that gephyrin contributes to the maintenance of GABAergic synapses in adult hippocampal DG neurons. The decreases in $GABA_AR\gamma2$ and VGAT densities observed in DG-specific gephyrin-KO

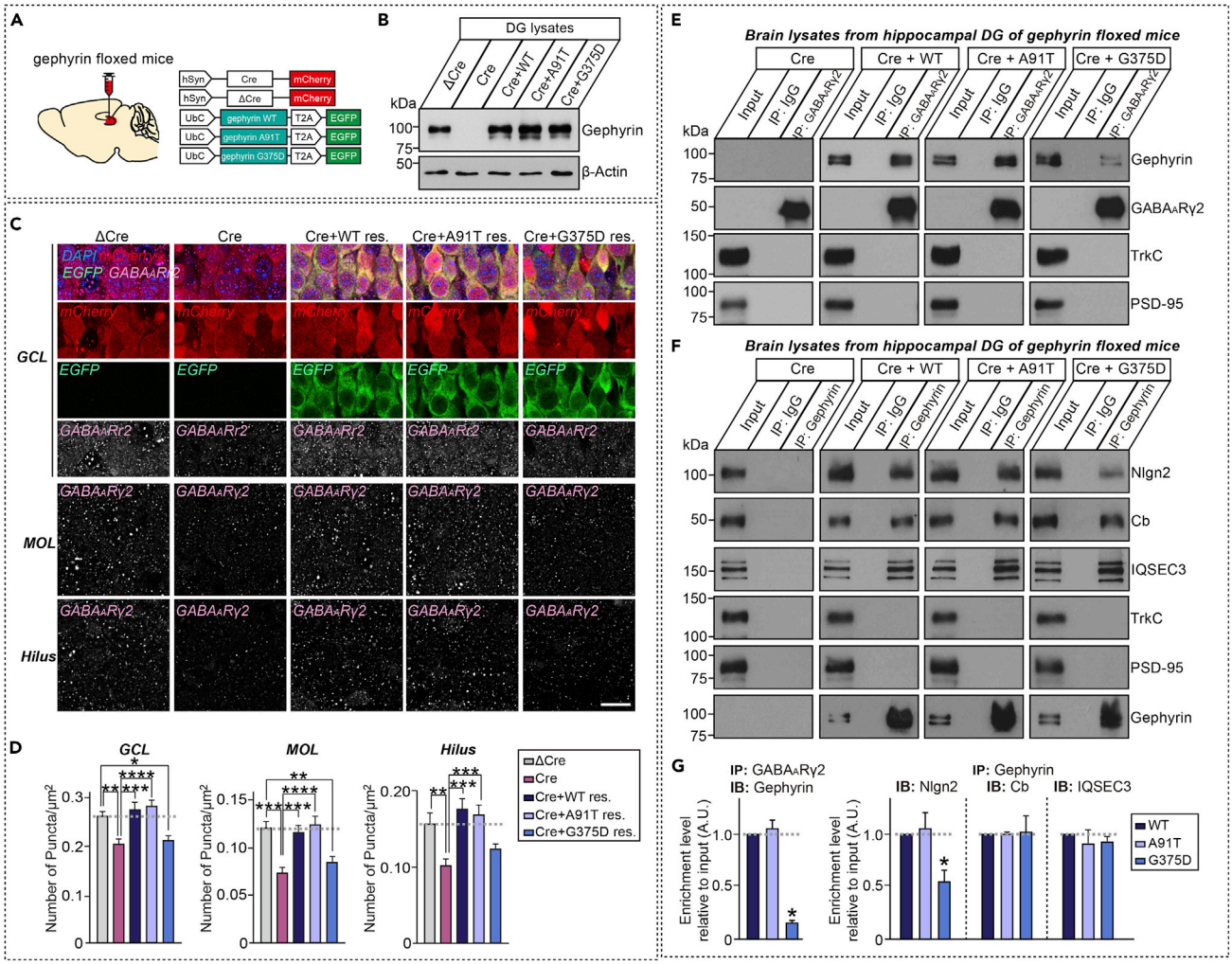

Figure 3. Gephyrin G375D impairs promotion of GABAergic synapse maintenance *in vivo*

(A) Schematic diagram of AAV vectors expressing Cre or ΔCre and WT gephyrin and its mutants (A91T and G375D) used for stereotactic injection into the DG of gephyrin floxed mice.

(B) Immunoblotting analyses with gephyrin antibodies validating gephyrin knockout and expression of gephyrin rescue constructs *in vivo*. Lysates from mouse brains stereotactically injected with AAVs were collected and immunoblotted with anti-gephyrin antibodies. An anti-β-actin antibody was used as a normalization control.

(C) Representative images showing $GABA_AR\gamma2^+$ puncta in the DG of mice stereotactically injected with the indicated AAVs. Scale bar, 20 μm (applies to all images). Abbreviations: MOL, molecular layer; GCL, granule cell layer.

(D) Quantification of the density of $GABA_AR\gamma2^+$ puncta per tissue area. Data are presented as means ± SEMs (n = 4 mice each after averaging data from 5 sections/mouse; *p < 0.05, **p < 0.01, ***p < 0.001, ****p < 0.0001; non-parametric ANOVA with Kruskal-Wallis test followed by *post hoc* Dunn's multiple comparison test).

(E) Synaptosomal fractions of adult brains from gephyrin floxed mice stereotactically injected with the indicated AAV viruses were immunoprecipitated with anti-$GABA_AR\gamma2$ antibodies and immunoblotted with anti-$GABA_AR\gamma2$, anti-gephyrin, anti-TrkC or anti-PSD-95 antibodies. An equal amount of rabbit IgG was used as a negative control. Input, 5%.

(F) Synaptosomal fractions of adult brains from gephyrin floxed mice stereotactically injected with the indicated AAV viruses were immunoprecipitated with an anti-gephyrin antibody and immunoblotted with the indicated antibodies. An equal amount of mouse IgG was used as a negative control. Input, 5%.

(G) Quantification of coimmunoprecipitated synaptic proteins in (E) or (F), normalized to controls. Data are means ± SEM from three independent experiments. (*p < 0.05; non-parametric Kruskal-Wallis test with Dunn's *post hoc* test).

mice were both rescued by expression of gephyrin WT or A91T but not by expression of mutant G375D (Figure 3C, 3D, and S5). These results indicate that the gephyrin mutation G375D, but not A91T, impairs the function of gephyrin in maintaining GABAergic synapse numbers *in vivo*.

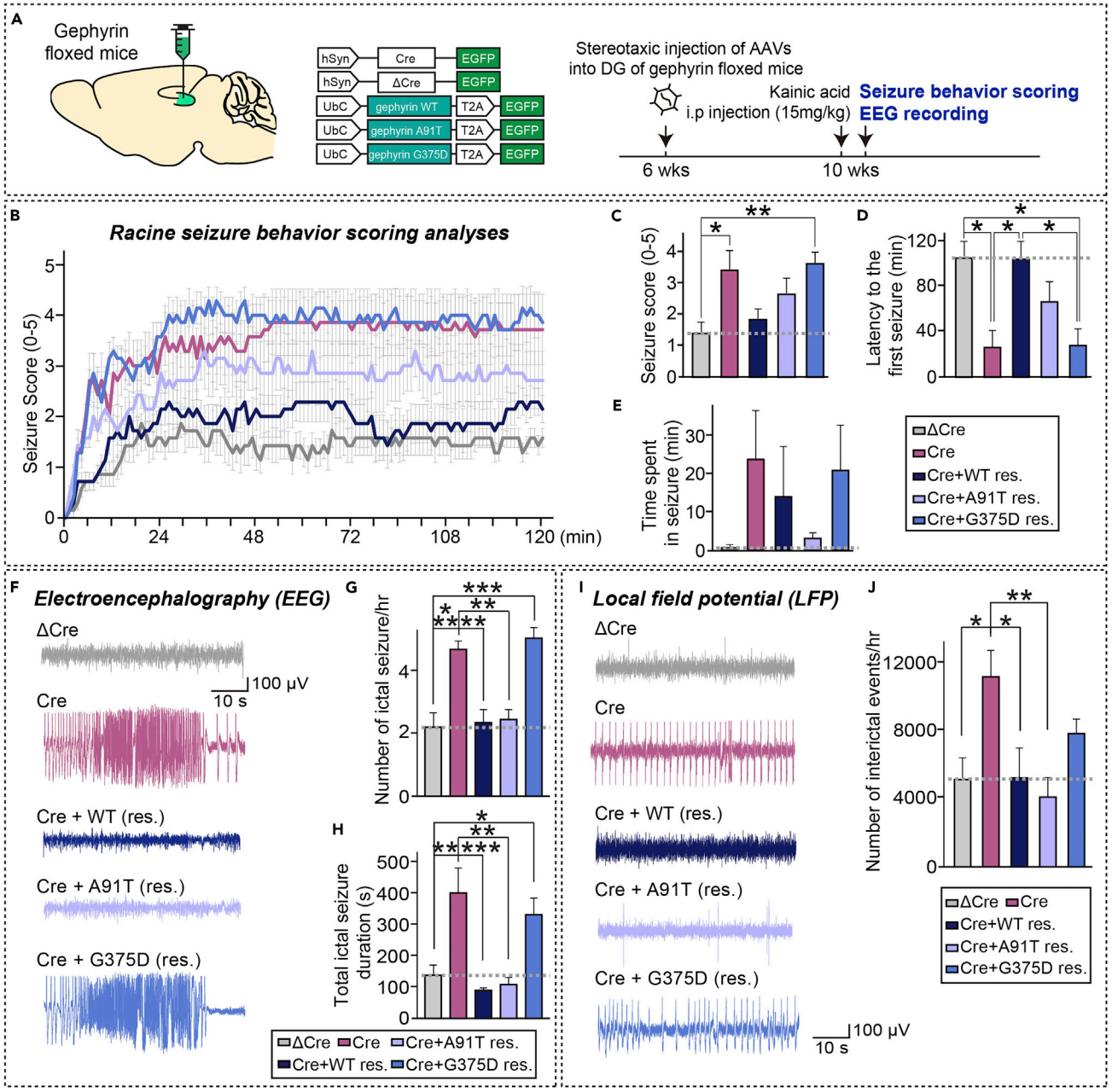

Figure 4. Gephyrin G375D mutant fails to rescue increased seizure susceptibility in DG-specific gephyrin-cKO mice

(A) Schematic diagram of AAV vectors expressing Cre or ΔCre and WT gephyrin or its mutants (A91T and G375D) used for stereotactic injection into the DG of gephyrin floxed mice. Experimental scheme for seizure scoring and EEG recordings. The DG region of the hippocampus of ~6-week-old gephyrin floxed mice was bilaterally injected with AAVs-ΔCre or Cre, or co-injected with Cre- and gephyrin-WT–expressing AAVs (Cre + WT res.) or gephyrin-mutant–expressing AAVs (Cre + A91T res. or Cre + G375D res.). Mice were intraperitoneally administered KA 2 weeks after AAV injections, after which seizures were scored and EEGs were recorded.

(B) KA-induced seizures in mice injected with the indicated AAVs were scored every 3 min for a total of 120 min, as described in Supplemental Information. Data are presented as means ± SEMs (ΔCre, n = 7 mice; Cre, n = 7 mice; Cre + WT [res.], n = 7 mice; Cre + A91T [res.], n = 7 mice; and Cre + G375D [res.], n = 7 mice; *p < 0.05, **p < 0.01, ***p < 0.001 vs. control; Kruskal-Wallis test followed by Dunn's *post hoc* test).

(C) Quantification of mean score values under each experimental condition. Data are presented as means ± SEMs (n = 7 mice/condition; *p < 0.05, **p < 0.01 vs. control; Kruskal-Wallis test followed by Dunn's *post hoc* test).

(D) Quantification of latency to the first seizure after KA administration under each condition. Data are presented as means ± SEMs (n = 7 mice/condition; *p < 0.05; Kruskal-Wallis test followed by Dunn's *post hoc* test).

(E) Quantification of time spent in seizure under each condition. Data are presented as means ± SEMs (n = 7 mice/condition).

Figure 4. *Continued*

(F) Representative EEG traces of ictal-like seizures recorded from the cortex under the indicated experimental conditions.

(G and H) Quantification of the number of ictal-like seizures (G) and total duration of ictal-like seizures (H) per hour under each condition. Data are presented as means ± SEMs (n = 8–11 mice/condition; *p < 0.05, **p < 0.01, ***p < 0.001 vs. control; Kruskal-Wallis test followed by Dunn's *post hoc* test).

(I) Representative LFP traces of inter-ictal events recorded from the DG under the indicated experimental conditions.

(J) Quantification of the number of inter-ictal events under each condition. Data are presented as means ± SEMs (n = 5–6 mice/condition; *p < 0.05, **p < 0.01 vs. control; Kruskal-Wallis test followed by Dunn's *post hoc* test).

To substantiate whether A91T or G375D mutations affect interactions of gephyrin with known binding proteins (Choii and Ko, 2015), we performed coimmunoprecipitation analyses using hippocampal DG lysates from gephyrin-KO mice expressing Cre-recombinase and/or gephyrin WT, A91T, or G375D. These analyses revealed that $GABA_AR\gamma2$ bound WT gephyrin or A91T to a similar extent but showed much less binding to G375D (Figures 3E and 3G). Similarly, association of the GABAergic synapse-specific adhesion protein, Nlgn2, with gephyrin G375D was significantly reduced compared with that of WT or A91T (Figures 3F and 3G). In contrast, amounts of the established gephyrin interaction partners, collybistin (Cb) and IQSEC3, were not affected by either gephyrin missense mutation, suggesting that the G375D mutation selectively disengages gephyrin from $GABA_A$ receptors and Nlgn2 *in vivo*. Control coimmunoprecipitation experiments performed in parallel showed no association of $GABA_AR\gamma2$ or gephyrin with TrkC or PSD-95- (Figures 3E and 3F).

Gephyrin G375D fails to normalize enhanced seizure susceptibility induced by a gephyrin deficiency

We next sought to determine whether gephyrin G375D influences epileptogenicity. To this end, we employed an acute kainic acid (KA)-induced epileptic mouse model in which mice stereotactically injected with the indicated AAVs were intraperitoneally administered KA (15 mg/kg), and then monitored for seizure-related behaviors by video recording (Figure 4A). The severity of KA-induced convulsive seizures was assessed by scoring responses using a revised Racine's scale, which ranks behavior from 0 (no abnormal behavior) to 5 (death) (Racine, 1972) (Figures 4B–4E). In keeping with a previous report that gephyrin deletion in forebrain neurons induces severe seizures (O'Sullivan et al., 2016), average seizure scores for 120 min after KA administration were ~2.45 fold higher in DG-specific gephyrin-KO mice than in control mice (Figures 4B and 4C). The increased seizure susceptibility observed in gephyrin-KO mice was largely normalized by coexpression of gephyrin WT and, to a lesser extent, by coexpression of A91T, but not G375D (Figures 4B–4E). In addition, gephyrin-KO mice exhibited a shorter seizure latency and prolonged seizure duration, effects that were also reduced or abolished by expression of gephyrin WT or A91T, but not G375D (Figures 4Dand 4E).

In line with these differential behavioral responses, electroencephalography (EEG) and local field potential (LFP) recordings revealed higher-amplitude and longer-lasting KA-induced ictal activity in DG-specific gephyrin-KO mice compared with control mice (Figures 4F–4J). The number of ictal seizure events per hour and total ictal seizure duration, determined from EEG activity, were significantly increased in gephyrin-KO mice compared with control mice, effects that were again completely rescued by expression of gephyrin WT or A91T but not G375D (Figures 4F–4H). Moreover, the number of inter-ictal spikes, quantified from 240 min of LFP recordings, was higher in DG-specific gephyrin-KO mice than in control mice (Figures 4I and 4J). This increased frequency of inter-ictal spikes in DG-specific gephyrin-KO mice was similarly normalized by expression of gephyrin WT or A91T, but not G375D (Figures 4I and 4J). Taken together, these results indicate that the gephyrin G375D mutation compromises the excitation/inhibition balance of hippocampal neuron activity *in vivo*.

DISCUSSION

In the present study, we applied MD simulations to predict the possible structural alterations produced by disease-associated point mutations that might be responsible for impairing the ability of gephyrin to form proper synaptic scaffolds. Of the six point mutations examined, A91T and G375D displayed reduced binding free energies for G-domain trimerization and E-domain dimerization, respectively, and failed to enhance the density of GABAergic synapses in cultured neurons, and hence were selected for extensive functional analyses. G375D, but not A91T, consistently exhibited loss-of-function phenotypes in all experimental settings. Although a previous report proposed impaired synaptic localization and decreased receptor binding as the mechanistic basis for the pathogenicity of the G375D mutant (Dejanovic et al., 2015), the present study provides a direct demonstration of the impact of this mutation on various gephyrin

functions *in vivo*, including higher-order oligomer formation, interactions with key proteins of GABAergic synapses, and neuronal activity in the hippocampal DG area.

Our atomic-scale MD simulations indicated that the G375D mutation does not affect the structure of gephyrin in the E-domain dimer, but selectively reduces the binding free energy of the E-domain dimer compared with WT gephyrin (Figure 1). This implies that gephyrin G375D scaffolds are less stable than those formed by the WT protein, an interpretation consistent with the markedly reduced ability of G375D to form large intracellular aggregates upon expression in COS-7 cells (Figures 2C and 2D).

We found no synapse-promoting effects of G375D at GABAergic synapses in cultured hippocampal neurons (Figure 2). This result is consistent with the previously reported diffuse cytosolic distribution of gephyrin G375D in these cells (Dejanovic et al., 2015). We further observed that, in contrast to the case for gephyrin WT and A91T, overexpression of G375D in the hippocampal DG area of mice carrying floxed gephyrin alleles failed to rescue the region-specific loss of GABAergic synapses induced by Cre expression (Figures 3, S4 and S5). Similarly, the G375D mutant failed to normalize the increased susceptibilities to KA-induced seizures and abnormal epileptiform discharges observed in hippocampal DG-specific gephyrin-KO mice, whereas these pathophysiological phenotypes were rescued by gephyrin WT and A91T (Figure 4). Functional deficits at GABAergic synapses and reduced enzymatic activity of gephyrin have been proposed to account for G375D-mediated dysfunctions of gephyrin (Dejanovic et al., 2015). In the current study, we provide compelling evidence to support the conclusion that G375D influences the 'structural' integrity of gephyrin-containing protein complexes, as initially predicted by supercomputing-based simulations (Figure 1). However, we found no evidence for dominant-negative effects of G375D in cultured hippocampal neurons as reported by Dejanovic et al., 2015 (Figure 2), although it remains to be tested whether a lack of the dominant-negative effects by G375D mutation is also observed *in vivo*. Notably, using circular dichroism analyses, Dejanovic et al. found that bacterially produced recombinant gephyrin G375D proteins showed no folding defects (Dejanovic et al., 2015). In contrast, our results, obtained by transiently transfecting mammalian gephyrin G375D into HEK293T cells, unambiguously demonstrated impaired multimer formation of gephyrin, as revealed by semi-quantitative gel filtration analyses (Figures 1I and 1J). Because gephyrin is proposed to act as a scaffold that is critical for binding to and anchoring of other GABAergic synaptic proteins, including $GABA_A$Rs, impaired formation of hexagonal lattices caused by the presence of G375D mutations might contribute to disorganization of GABAergic synapse structure, function and, possibly, plasticity (Alvarez, 2017; Choii and Ko, 2015; Groeneweg et al., 2018; Pizzarelli et al., 2019). To the best of our knowledge, this study is the first to test whether and how gephyrin missense mutations associated with neurological disorders contribute to dysregulation of structural and functional aspect of *in vivo* synapses. Although our various analyses did not reveal any structural or functional phenotypes for the other gephyrin missense mutations examined, the possibility remains that these mutations contribute to gephyrin-associated pathophysiology via as-yet unidentified mechanism(s).

Gephyrin interacts with various other synaptic proteins expressed exclusively at GABAergic synapses, such as GlyRs, the $GABA_A$ receptor α3 subunit, Cbs, Nlgn2, GABARAP, Pin1, and IQSEC3, to coordinate inhibitory postsynaptic organization (Alvarez, 2017; Choii and Ko, 2015; Groeneweg et al., 2018; Pizzarelli et al., 2019). Armed with newly available antibodies specific for a subset of gephyrin-binding proteins (i.e. Cbs, Nlgn2 and IQSEC3), we examined whether gephyrin mutations influence the association of gephyrin with these proteins *in vivo*. Consistent with results from other assays, G375D, but not A91T, disengaged synaptic $GABA_A$ receptors (monitored using $GABA_A R\gamma 2$ antibodies) and Nlgn2, but not Cbs or IQSEC3, from gephyrin-containing complexes in hippocampal DG neurons (Figure 3). Although further in-depth analyses are required, our findings suggest that the G375D mutation likely induces structural changes in the E-domain of gephyrin, where the Gly375 residue is located, further influencing association with $GABA_A$ receptors and Nlgn2. Because gephyrin binds Cbs and IQSEC3 through residues 319–329 and the G-domain, respectively (Kins et al., 2000; Um et al., 2016), it is plausible that G375D might exert little or no effect on interactions with Cbs and IQSEC3. On the other hand, because previous structural modeling and atomic force microscopy studies reported that gephyrin exists predominantly in a trimeric form (Sander et al., 2013), we are unable to completely rule out the possibility that G375D might affect gephyrin-binding affinity for Nlgn2 or $GABA_A$ receptors. Whether G375D negatively affects GABAergic synaptic strength and postsynaptic assembly, in line with previous reports on the roles of gephyrin/Nlgn2 interaction (Antonelli et al., 2014; Poulopoulos et al., 2009), remains to be determined.

Diverse gephyrin mutations continue to be identified in human patients with variable neurological features and distinct neuropsychiatric disorders (Ko et al., 2015). Consistent with this, deletion of gephyrin selectively in forebrain mouse neurons markedly reduces $GABA_A$R-positive puncta in the hippocampus and cortex, together with increased anxiety-like behavior and increased lethality presumably owing to prevalent epileptic seizures (O'Sullivan et al., 2016). Our results further showed that the loss of gephyrin in the hippocampal DG was sufficient to trigger epileptic seizures (Figure 4). The immediate goals of future studies should be to use conditional heterozygous gephyrin G375D knock-in mice to address whether G375D exhibits similar or distinct behavioral abnormalities compared with gephyrin forebrain cKO mice. In addition, considering the robustness of the effects of the G375D mutation, it would be extremely interesting to introduce induced neuronal cells, with the goal of replicating gephyrin G375D-associated disease phenotypes in human neurons.

Limitations of the study

The current study clearly demonstrated that the gephyrin mutation, G375D, has impact on various gephyrin functions, including higher-order oligomer formation, interactions with Nlgn2 or $GABA_A$ receptors, or network activity. However, it remains to be determined how other gephyrin mutations contribute to gephyrin-associated pathologies. In addition, it remains to be tested whether the lack of dominant-negative effects observed for G375D mutation is recapitulated *in vivo*. Lastly, future studies on higher-order oligomer formation of gephyrin *in vivo* are warranted to support the significance and mechanisms of G375D mutant-associated pathologies reported in the current study.

Resource availability

Lead contact

Further information and requests for resources and reagents should be directed to and will be fulfilled by the Lead Contact, Ji Won Um (jiwonum@dgist.ac.kr).

Materials availability

All unique/stable reagents generated in this study are available from the Lead contact upon reasonable request and with a completed Materials Transfer Agreement.

Data and code availability

This study did not generate data sets.

METHODS

All methods can be found in the accompanying Transparent Methods supplemental file.

SUPPLEMENTAL INFORMATION

Supplemental Information can be found online at https://doi.org/10.1016/j.isci.2021.102037.

ACKNOWLEDGMENTS

We are grateful to Jinha Kim (DGIST) for technical assistance. This work was supported by grants from the DGIST R&D Program of the Ministry of Science, ICT & Future Planning (20-CoE-BT-01 to M.K., J.K., I.C. and J.W.U.), the DGIST Start-up Fund Program of the Ministry of Science, ICT and Future Planning (2020010058 to J.W.U.) and the Brain Research Program through the National Research Foundation funded by the Ministry of Science, ICT & Future Planning (2020R1A4A1019009 to J.W.U. and 2017M3C7A1023470 to J.K.). We also acknowledge the Supercomputing Bigdata Center (DGIST) for their dedicated allocation of supercomputing resources, and the Core Protein Resources Center (DGIST) for supporting experiments.

AUTHOR CONTRIBUTIONS

J.K., I.C., and J.W.U. conceived the project; S.K. and D.P. performed the experiments; M.K. performed simulations; A-.R.L. and H.B. provided key experimental reagents; S.K., M.K., D.P., J.K., and J.W.U. analyzed the data; and S.K., M.K., H.B., J.K., I.C., and J.W.U. wrote the manuscript.

DECLARATION OF INTERESTS

The authors declare that they have no conflicts of interest.

Received: August 4, 2020
Revised: December 1, 2020
Accepted: January 4, 2021
Published: February 19, 2021

REFERENCES

Agarwal, S., Tannenberg, R.K., and Dodd, P.R. (2008). Reduced expression of the inhibitory synapse scaffolding protein gephyrin in Alzheimer's disease. J. Alzheimers Dis. *14*, 313–321.

Alvarez, F.J. (2017). Gephyrin and the regulation of synaptic strength and dynamics at glycinergic inhibitory synapses. Brain Res. Bull. *129*, 50–65.

Anastasia, A., Deinhardt, K., Chao, M.V., Will, N.E., Irmady, K., Lee, F.S., Hempstead, B.L., and Bracken, C. (2013). Val66Met polymorphism of BDNF alters prodomain structure to induce neuronal growth cone retraction. Nat. Commun. *4*, 2490.

Antonelli, R., Pizzarelli, R., Pedroni, A., Fritschy, J.M., Del Sal, G., Cherubini, E., and Zacchi, P. (2014). Pin1-dependent signalling negatively affects GABAergic transmission by modulating neuroligin2/gephyrin interaction. Nat. Commun. *5*, 5066.

Bath, K.G., and Lee, F.S. (2006). Variant BDNF (Val66Met) impact on brain structure and function. Cogn. Affect. Behav. Neurosci. *6*, 79–85.

Betz, H. (1998). Gephyrin, a major player in GABAergic postsynaptic membrane assembly? Nat. Neurosci. *1*, 541–543.

Calamai, M., Specht, C.G., Heller, J., Alcor, D., Machado, P., Vannier, C., and Triller, A. (2009). Gephyrin oligomerization controls GlyR mobility and synaptic clustering. J. Neurosci. *29*, 7639–7648.

Choii, G., and Ko, J. (2015). Gephyrin: a central GABAergic synapse organizer. Exp. Mol. Med. *47*, e158.

Dejanovic, B., Djemie, T., Grunewald, N., Suls, A., Kress, V., Hetsch, F., Craiu, D., Zemel, M., Gormley, P., Lal, D., et al. (2015). Simultaneous impairment of neuronal and metabolic function of mutated gephyrin in a patient with epileptic encephalopathy. EMBO Mol. Med. *7*, 1580–1594.

Dejanovic, B., Lal, D., Catarino, C.B., Arjune, S., Belaidi, A.A., Trucks, H., Vollmar, C., Surges, R., Kunz, W.S., Motameny, S., et al. (2014). Exonic microdeletions of the gephyrin gene impair GABAergic synaptic inhibition in patients with idiopathic generalized epilepsy. Neurobiol. Dis. *67*, 88–96.

Falivelli, G., De Jaco, A., Favaloro, F.L., Kim, H., Wilson, J., Dubi, N., Ellisman, M.H., Abrahams, B.S., Taylor, P., and Comoletti, D. (2012). Inherited genetic variants in autism-related CNTNAP2 show perturbed trafficking and ATF6 activation. Hum. Mol. Genet. *21*, 4761–4773.

Feng, G., Tintrup, H., Kirsch, J., Nichol, M.C., Kuhse, J., Betz, H., and Sanes, J.R. (1998). Dual requirement for gephyrin in glycine receptor clustering and molybdoenzyme activity. Science *282*, 1321–1324.

Forstera, B., Belaidi, A.A., Juttner, R., Bernert, C., Tsokos, M., Lehmann, T.N., Horn, P., Dehnicke, C., Schwarz, G., and Meier, J.C. (2010). Irregular RNA splicing curtails postsynaptic gephyrin in the cornu ammonis of patients with epilepsy. Brain *133*, 3778–3794.

Fritschy, J.M., Harvey, R.J., and Schwarz, G. (2008). Gephyrin: where do we stand, where do we go? Trends Neurosci. *31*, 257–264.

Groeneweg, F.L., Trattnig, C., Kuhse, J., Nawrotzki, R.A., and Kirsch, J. (2018). Gephyrin: a key regulatory protein of inhibitory synapses and beyond. Histochem. Cell Biol. *150*, 489–508.

Heinzen, E.L., Neale, B.M., Traynelis, S.F., Allen, A.S., and Goldstein, D.B. (2015). The genetics of neuropsychiatric diseases: looking in and beyond the exome. Annu. Rev. Neurosci. *38*, 47–68.

Kang, H., Han, K.A., Won, S.Y., Kim, H.M., Lee, Y.H., Ko, J., and Um, J.W. (2016). Slitrk missense mutations associated with neuropsychiatric disorders distinctively impair Slitrk trafficking and synapse formation. Front. Mol. Neurosci. *9*, 104.

Kim, E.Y., Schrader, N., Smolinsky, B., Bedet, C., Vannier, C., Schwarz, G., and Schindelin, H. (2006). Deciphering the structural framework of glycine receptor anchoring by gephyrin. EMBO J. *25*, 1385–1395.

Kins, S., Betz, H., and Kirsch, J. (2000). Collybistin, a newly identified brain-specific GEF, induces submembrane clustering of gephyrin. Nat. Neurosci. *3*, 22–29.

Kirsch, J., Wolters, I., Triller, A., and Betz, H. (1993). Gephyrin antisense oligonucleotides prevent glycine receptor clustering in spinal neurons. Nature *366*, 745–748.

Kiss, E., Gorgas, K., Schlicksupp, A., Gross, D., Kins, S., Kirsch, J., and Kuhse, J. (2016). Biphasic alteration of the inhibitory synapse scaffold protein gephyrin in early and late stages of an alzheimer disease model. Am. J. Pathol. *186*, 2279–2291.

Kneussel, M., and Betz, H. (2000). Clustering of inhibitory neurotransmitter receptors at developing postsynaptic sites: the membrane activation model. Trends Neurosci. *23*, 429–435.

Ko, J., Choii, G., and Um, J.W. (2015). The balancing act of GABAergic synapse organizers. Trends Mol. Med. *21*, 256–268.

Lionel, A.C., Vaags, A.K., Sato, D., Gazzellone, M.J., Mitchell, E.B., Chen, H.Y., Costain, G., Walker, S., Egger, G., Thiruvahindrapuram, B., et al. (2013). Rare exonic deletions implicate the synaptic organizer Gephyrin (GPHN) in risk for autism, schizophrenia and seizures. Hum. Mol. Genet. *22*, 2055–2066.

Maric, H.M., Kasaragod, V.B., Hausrat, T.J., Kneussel, M., Tretter, V., Stromgaard, K., and Schindelin, H. (2014). Molecular basis of the alternative recruitment of GABA(A) versus glycine receptors through gephyrin. Nat. Commun. *5*, 5767.

Medland, S.E., Jahanshad, N., Neale, B.M., and Thompson, P.M. (2014). Whole-genome analyses of whole-brain data: working within an expanded search space. Nat. Neurosci. *17*, 791–800.

O'Sullivan, G.A., Jedlicka, P., Chen, H.X., Kalbouneh, H., Ippolito, A., Deller, T., Nawrotzki, R.A., Kuhse, J., Kalaidzidis, Y.L., Kirsch, J., et al. (2016). Forebrain-specific loss of synaptic GABAA receptors results in altered neuronal excitability and synaptic plasticity in mice. Mol. Cell. Neurosci. *72*, 101–113.

Pizzarelli, R., Griguoli, M., Zacchi, P., Petrini, E.M., Barberis, A., Cattaneo, A., and Cherubini, E. (2019). Tuning GABAergic inhibition: gephyrin molecular organization and functions. Neuroscience *439*, 125–136.

Poulopoulos, A., Aramuni, G., Meyer, G., Soykan, T., Hoon, M., Papadopoulos, T., Zhang, M., Paarmann, I., Fuchs, C., Harvey, K., et al. (2009). Neuroligin 2 drives postsynaptic assembly at perisomatic inhibitory synapses through gephyrin and collybistin. Neuron *63*, 628–642.

Racine, R.J. (1972). Modification of seizure activity by electrical stimulation. I. After-discharge threshold. Electroencephalogr Clin. Neurophysiol. *32*, 269–279.

Riccardi, F., Urquhart, J., McCullagh, G., Lawrence, P., and Douzgou, S. (2019). A patient with a novel CNTNAP2 homozygous variant: further delineation of the CASPR2 deficiency syndrome and review of the literature. Clin. Dysmorphol. *28*, 66–70.

Saiyed, T., Paarmann, I., Schmitt, B., Haeger, S., Sola, M., Schmalzing, G., Weissenhorn, W., and Betz, H. (2007). Molecular basis of gephyrin clustering at inhibitory synapses: role of G- and E-domain interactions. J. Biol. Chem. *282*, 5625–5632.

Sander, B., Tria, G., Shkumatov, A.V., Kim, E.Y., Grossmann, J.G., Tessmer, I., Svergun, D.I., and Schindelin, H. (2013). Structural characterization of gephyrin by AFM and SAXS reveals a mixture

of compact and extended states. Acta Crystallogr. D Biol. Crystallogr. *69*, 2050–2060.

Schwarz, G., Schrader, N., Mendel, R.R., Hecht, H.J., and Schindelin, H. (2001). Crystal structures of human gephyrin and plant Cnx1 G domains: comparative analysis and functional implications. J. Mol. Biol. *312*, 405–418.

Sestan, N., and State, M.W. (2018). Lost in translation: traversing the complex path from genomics to therapeutics in autism spectrum disorder. Neuron *100*, 406–423.

Sola, M., Bavro, V.N., Timmins, J., Franz, T., Ricard-Blum, S., Schoehn, G., Ruigrok, R.W., Paarmann, I., Saiyed, T., O'Sullivan, G.A., et al. (2004). Structural basis of dynamic glycine receptor clustering by gephyrin. EMBO J. *23*, 2510–2519.

Sola, M., Kneussel, M., Heck, I.S., Betz, H., and Weissenhorn, W. (2001). X-ray crystal structure of the trimeric N-terminal domain of gephyrin. J. Biol. Chem. *276*, 25294–25301.

Stallmeyer, B., Schwarz, G., Schulze, J., Nerlich, A., Reiss, J., Kirsch, J., and Mendel, R.R. (1999). The neurotransmitter receptor-anchoring protein gephyrin reconstitutes molybdenum cofactor biosynthesis in bacteria, plants, and mammalian cells. Proc. Natl. Acad. Sci. U S A *96*, 1333–1338.

State, M.W., and Levitt, P. (2011). The conundrums of understanding genetic risks for autism spectrum disorders. Nat. Neurosci. *14*, 1499–1506.

Südhof, T.C. (2017). Synaptic neurexin complexes: a molecular code for the logic of neural circuits. Cell *171*, 745–769.

Tyagarajan, S.K., and Fritschy, J.M. (2014). Gephyrin: a master regulator of neuronal function? Nat. Rev. Neurosci. *15*, 141–156.

Um, J.W., Choii, G., Park, D., Kim, D., Jeon, S., Kang, H., Mori, T., Papadopoulos, T., Yoo, T., Lee, Y., et al. (2016). IQ Motif and SEC7 domain-containing protein 3 (IQSEC3) interacts with gephyrin to promote inhibitory synapse formation. J. Biol. Chem. *291*, 10119–10130.

iScience, Volume *24*

Supplemental Information

Impaired formation of high-order gephyrin oligomers underlies gephyrin dysfunction-associated pathologies

Seungjoon Kim, Mooseok Kang, Dongseok Park, Ae-Ree Lee, Heinrich Betz, Jaewon Ko, Iksoo Chang, and Ji Won Um

SUPPLEMENTAL FIGURES

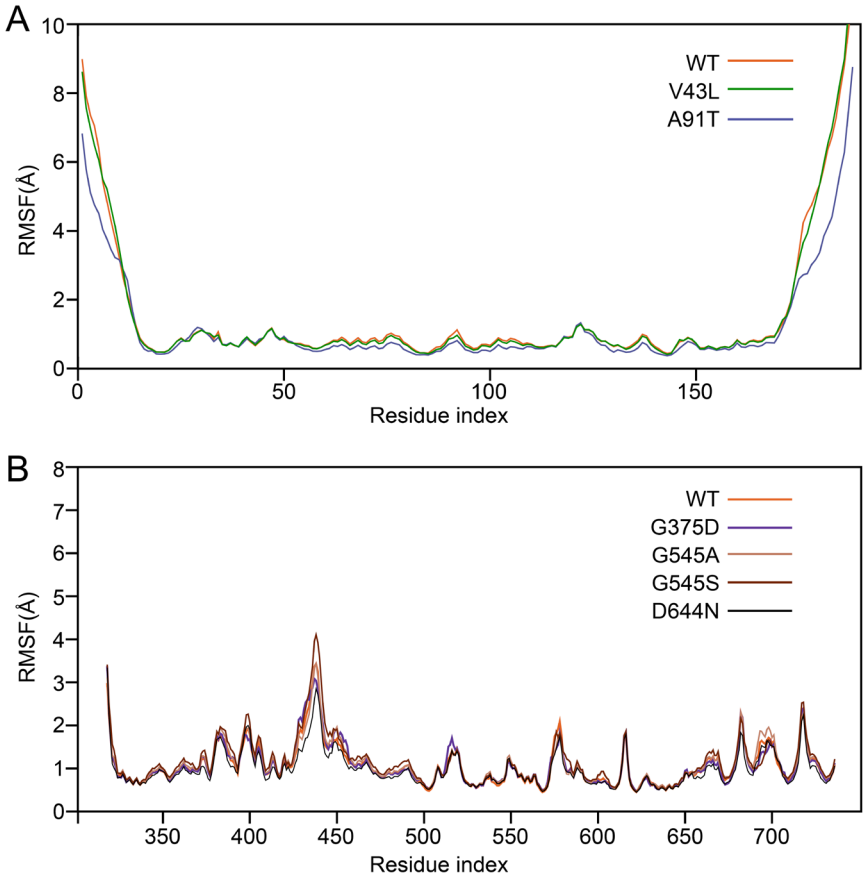

Supplemental Figure S1. Root-Mean-Square-Fluctuation (RMSF) of the Coordinate for Residues in Structures of Gephyrin WT and Mutants by MD Simulation (Related to *Figure 1*).

(**A**) Backbone RMSF of residues in the G-domain during a 0.5–1 μs time window from G-domain trimer MD simulation.

(**B**) Backbone RMSF of residues in the E-domain during a 0.5–1 μs time window from E-domain dimer MD simulation.

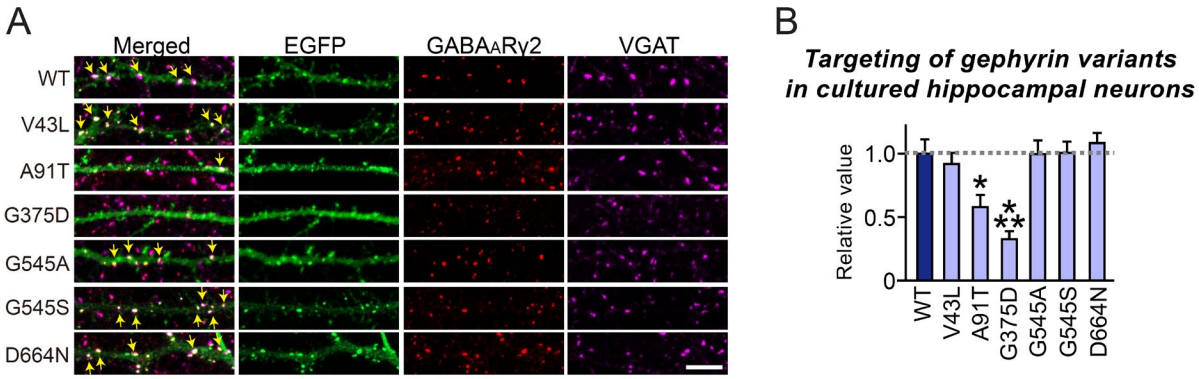

Supplemental Figure S2. GABAergic Synaptic Targeting of Gephyrin WT or Mutants in Cultured Hippocampal Neurons (Related to *Figure 2*).

(**A**) Representative images of cultured hippocampal neurons transfected at DIV10 with EGFP-tagged gephyrin WT or mutants, and analyzed at DIV14 by triple-immunofluorescence staining using anti-$GABA_AR\gamma2$ (red), anti-VGAT (magenta) and anti-EGFP (green) antibodies. Yellow arrows mark colocalization of gephyrin with both $GABA_AR\gamma2$ and VGAT puncta. Scale bar, 10 μm (applies to all images).

(**B**) Summary graphs showing inhibitory synaptic targeting of gephyrin variants in cultured hippocampal neurons. Data are presented as means ± SEMs from three independent experiments (2–3 dendrites per transfected neurons were analyzed and group-averaged; *$p < 0.05$, ***$p < 0.001$; non-parametric ANOVA with Kruskal-Wallis test followed by *post hoc* Dunn's multiple comparison test).

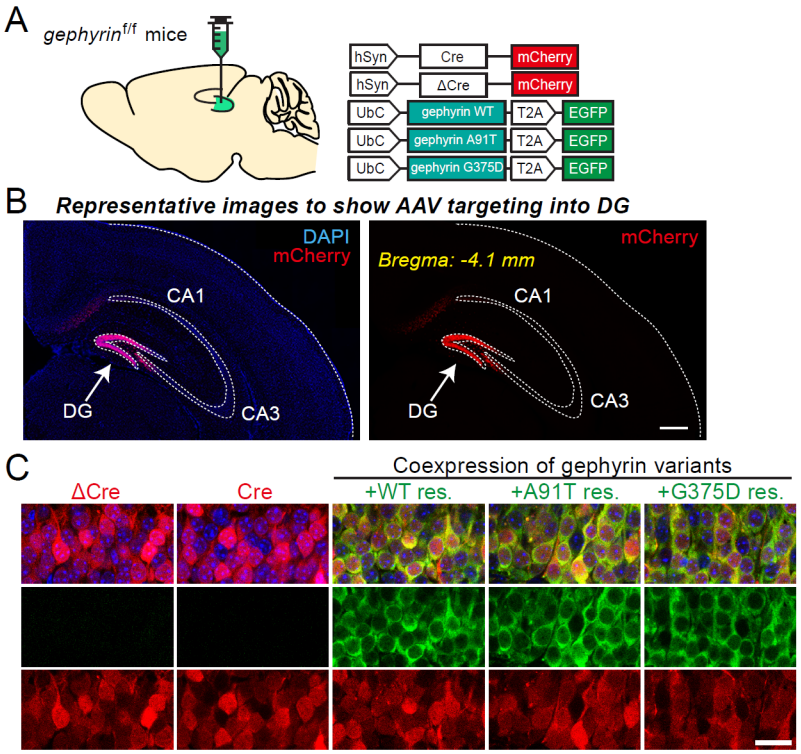

Supplemental Figure S3. Targeting of AAVs Expressing Gephyrin Variants into the Hippocampal DG of Gephyrin$^{f/f}$ Mice (Related to *Figures 3* and *4*).

(**A**) Schematic diagram of AAV vectors expressing Cre or ΔCre and WT gephyrin and its mutants (A91T and G375D) used for stereotactic injection into the DG of gephyrin floxed mice.

(**B**) Representative brain sections illustrating the precise targeting of adeno-associated virus (AAV) for expression of Cre recombinase in the DG. Scale bar: 500 μm.

(**C**) Representative images of hippocampal DG regions 2 weeks after stereotactic infection of gephyrin floxed mice with the indicated AAVs, followed by monitoring of infected neurons to validate the expression of rescue AAVs. Note that virus coinfection efficiency was 98.05 ± 0.70% for Cre and gephyrin WT, 97.58 ± 0.65% for Cre and gephyrin A91T, and 97.95 ± 0.79% for Cre and gephyrin G375D. Scale bar: 20 μm.

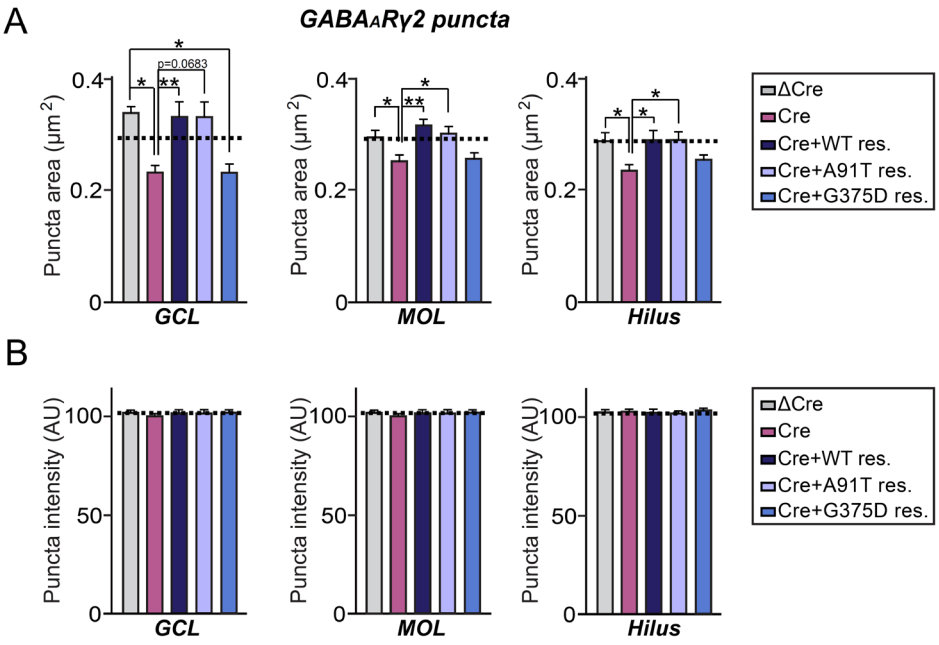

Supplemental Figure S4. Quantification of GABA$_A$Rγ2-positive Puncta Area and Intensity in Gephyrin-deficient DG Neurons (Related to *Figure 3*).

(**A** and **B**) Quantification of the size (**A**), and intensity (**B**) of GABA$_A$Rγ2$^+$ puncta. Data are presented as means ± SEMs (n = 4 mice/group after averaging data from 5 sections/mouse; *$p < 0.05$, **$p < 0.01$; non-parametric ANOVA with Kruskal-Wallis test followed by *post hoc* Dunn's multiple comparison test).

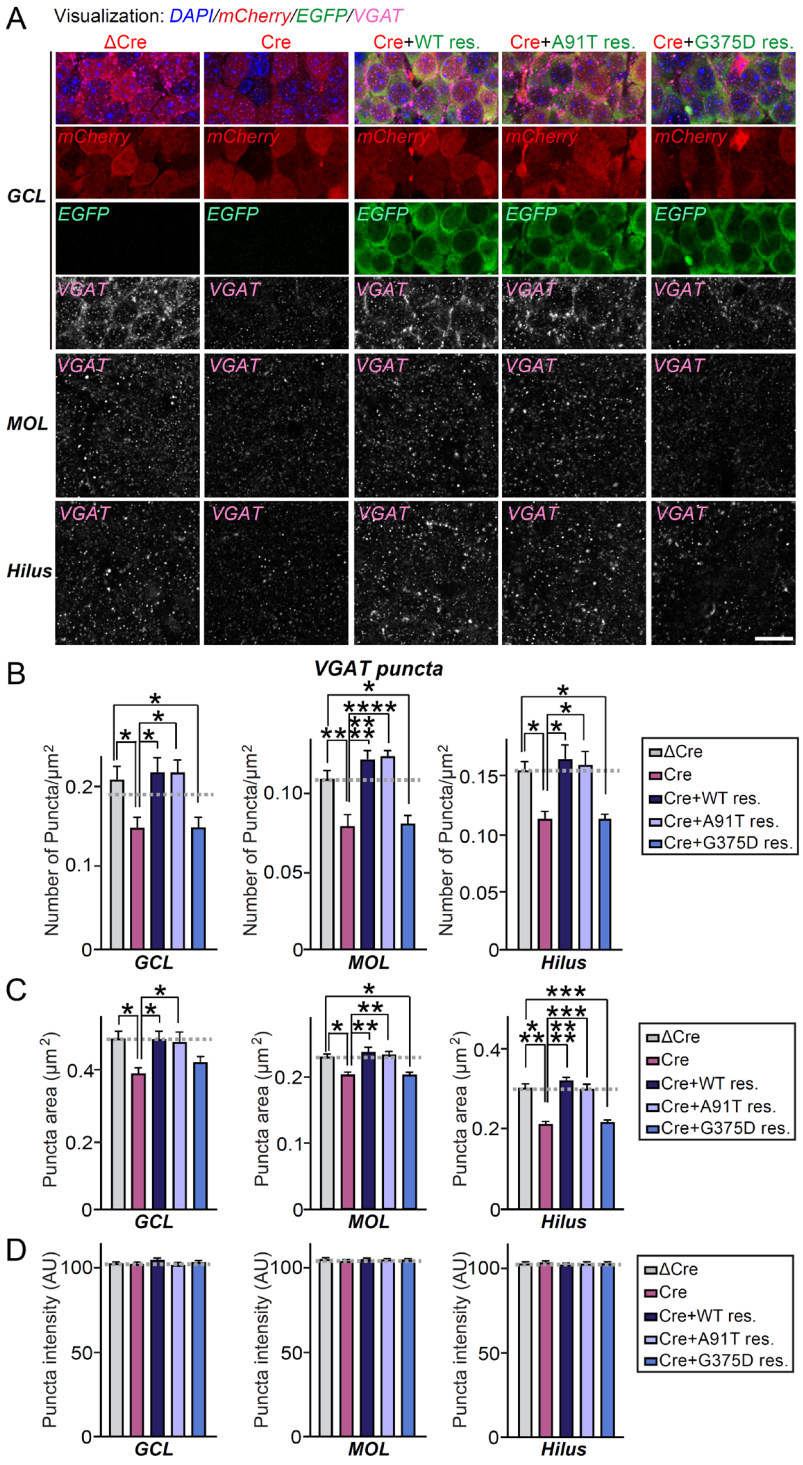

Supplemental Figure S5. Quantification of VGAT-positive Puncta in Gephyrin-deficient DG Neurons (Related to *Figure 3*).

(**A**) Representative images showing VGAT^{+} puncta in the DG of mice stereotactically injected with the indicated AAVs. Scale bar, 20 μm (applies to all images). Abbreviations: MOL, molecular layer; GCL, granule cell layer.

(**B-D**) Quantification of the density (**B**), size (**C**), and intensity (**D**) of VGAT+ puncta. Data are presented as means ± SEMs (n = 4 mice/group after averaging data from 5 sections/mouse; *$p < 0.05$, **$p < 0.01$, ***$p < 0.001$, ****$p < 0.0001$; non-parametric ANOVA with Kruskal-Wallis test followed by *post hoc* Dunn's multiple comparison test).

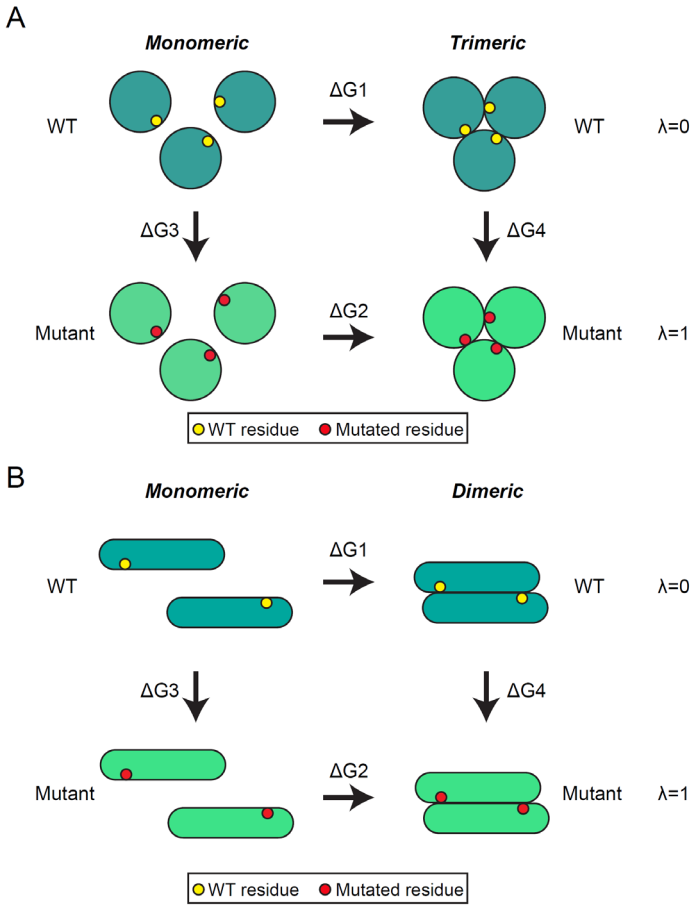

Supplemental Figure S6. Thermodynamic Cycle for Estimating Differences in Binding Free Energy, Calculated Using TI (Related to *Figure 1*).

(**A**) G-domain trimer.

(**B**) E-domain dimer.

TRANSPARENT METHODS

KEY RESOURES TABLE

REAGENT or RESOURCE	SOURCE	IDENTIFIER
Antibodies		
Rabbit polyclonal Anti-IQSEC3	Jaewon Ko's lab	JK079; RRID: AB_2687864
Mouse monoclonal Anti-Gephyrin	Synaptic Systems	Cat #147 111; RRID: AB_2619837
Rabbit monoclonal Anti-$GABA_AR\gamma2$	Synaptic Systems	Cat #224 003; RRID: AB_2263066
Rabbit polyclonal Anti-VGAT	Synaptic Systems	Cat #131 003; RRID: AB_887869
Mouse monoclonal Anti-VGAT	Synaptic Systems	Cat #131 011; RRID: AB_887868
Goat polyclonal Anti-EGFP	Rockland	Cat #ab5450; RRID: AB_218182
Rabbit polyclonal Anti-Nlgn2	Synaptic Systems	Cat#129 202; RRID: AB_993011
Rabbit polyclonal Anti-Collybistin	Synaptic Systems	Cat#261 003; RRID: AB_2619977
Rabbit monoclonal Anti-TrkC	Cell Signaling	C44H5; RRID: AB_2155283
Rabbit polyclonal Anti-PSD-95	Jaewon Ko's lab	JK016; RRID: AB_2722693
FITC-conjugated Donkey Anti-goat IgG antibody	Jackson ImmunoResearch Laboratories	Cat# 705-007-003; RRID: AB_2340403
Cy3-conjugated Donkey Anti-Rabbit IgG antibody	Jackson ImmunoResearch Laboratories	Cat #711-165-152; RRID: AB_2307443
Cy3-conjugated Donkey Anti-Mouse IgG antibody	Jackson ImmunoResearch Laboratories	Cat #715-165-150; RRID: AB_2340813
Alexa Fluor® 647-conjugated Goat Anti-mouse IgG antibody	ThermoFisher Scientific	Cat #A28181; RRID: AB_2536165
Alexa Fluor® 647-conjugated Goat Anti-rabbut IgG antibody	ThermoFisher Scientific	Cat #A27040; RRID: AB_2536101
Chemicals, Peptides, and Recombinant Proteins		
Kainic acid	Sigma	Cat #K0250
Neurobasal medium	ThermoFisher Scientific	Cat #21103049
B-27 supplement (50X)	ThermoFisher Scientific	Cat #17504-044
Penicillin/Streptomycin	ThermoFisher Scientific	Cat #15140122
HBSS (Hanks' Balanced Salt Solution)	ThermoFisher Scientific	Cat #14065056
GlutaMax Supplement	ThermoFisher Scientific	Cat #35050061
FBS (Fetal Bovine Serum)	WELGENE	Cat #PK004-01

Sodium pyruvate	ThermoFisher Scientific	Cat #11360070
Poly-D-lysine hydrobromide	Sigma	Cat #P0899
Vectashield mounting medium	Vector Laboratories	Cat #H-1200
2,2,2-Tribromoethyl alcohol	Sigma	Cat #T48402
Tert-Amyl alcohol	Sigma	Cat #240846
Experimental Models: Cell Lines		
Cultured neuronal cells (from rat embryos)	N/A	N/A
HEK 293T cells	ATCC	Cat # CRL-3216
Experimental Models: Organisms/Strains		
Mouse: Gephyrin floxed mice		O'Sullivan et al., 2016
Recombinant DNA		
L313-Ub-gephyrin WT	This study	N/A
L313-Ub-gephyrin A91T	This study	N/A
L313-Ub-gephyirn G375D	This study	N/A
pEGFP-C2-gephyrin WT	This study	N/A
pEGFP-C2-gephyrin A91T	This study	N/A
pEGFP-C2-gephyrin G375D	This study	N/A
pEGFP-C2-gephyrin G545A	This study	N/A
pEGFP-C2-gephyrin G545S	This study	N/A
pEGFP-C2-gephyrin D664N	This study	N/A
pAAV2/9-gephyrin WT-T2A-EGFP	This study	N/A
pAAV2/9-gephyrin A91T-T2A-EGFP	This study	N/A
pAAV2/9-gephyrin G375D-T2A-EGFP	This study	N/A
pAAV-hSyn-ΔCre-mCherry	A gift from Dr. Thomas Südhof (Stanford University)	N/A
pAAV-hSyn-Cre-mCherry	A gift from Dr. Thomas Südhof (Stanford University)	N/A
Software and Algorithms		
MetaMorph	Molecular Devices	https://www.moleculardevices.com
GraphPad Prism 7.0	GraphPad	https://www.graphpad.com
AMBER18	D.A. Case et al., 2018	http://ambermd.org/
VMD 1.9.3	Humphrey et al., 1996	https://www.ks.uiuc.edu/Research/vmd/

EXPERIMENTAL MODEL AND SUBJECT DETAILS

Cell Culture

HEK293T cells and COS7 cells were cultured in Dulbecco's Modified Eagle's Medium (DMEM; WELGENE) supplemented with 10% fetal bovine serum (FBS; Tissue Culture Biologicals) and 1% penicillin-streptomycin (Thermo Fisher) at 37 °C in a humidified 5% CO2 atmosphere. All procedures were performed according to the guidelines and protocols for rodent experimentation approved by the Institutional Animal Care and Use Committee of DGIST.

Animals

Conditional gephyrin knockout mice (gephyrinflox/flox) were previously described (O'Sullivan et al., 2016). Mice were housed and bred at the animal facility of Daegu Gyeongbuk Institute of Science and Technology (DGIST), and their experimental uses were approved by the Institutional Animal Care and Use Committee of DGIST. All C57BL/6N mice were maintained and handled in accordance with protocols (DGIST-IACUC-19052109-00) approved by the Institutional Animal Care and Use Committee of DGIST under standard, temperature-controlled laboratory conditions. All experimental procedures were performed on male mice. Pregnant rats (Daehan Biolink) were used to prepare in vitro cultures of dissociated hippocampal neurons. All procedures were conducted according to the guidelines and protocols for rodent experimentation approved by the Institutional Animal Care and Use Committee of DGIST. Mice were kept on a 12:12 light/dark cycle (lights on at 7:00 am), and received water and food ad libitum.

METHOD DETAILS

Construction of Gephyrin 3D Structures. Previously reported structures of the rat gephyrin G-domain monomer (PDB ID, 1IHC; UNP ID, Q03555; residues 2–188) (Sola et al., 2001), human gephyrin G-domain trimer (PDB ID, 1JLJ; UNP ID, Q9NQX3; residues 1–181) (Schwarz et al., 2001), and rat gephyrin E-domain dimer (PDB ID, 4TK1; UNP ID, Q03555; residues 318–736) (Maric et al., 2014) were used in MODELLER (Webb and Sali, 2016) to fill in 3D structures for missing residues and reconstruct the full structures of G-domain trimers and E-domain dimers. The locations of missing residues were at the N- and C-termini of both domains and residues 431-440 of the E-domain. After building the structure of missing residues, loops were refined with an automatic loop refinement module with using the 'refine.fast' option in MODELLER. The C-domain of gephyrin is intrinsically structurally disordered, and thus is not compatible with modeling and simulation. Thus, simulations were performed only for structured regions of gephyrin (i.e., G-domain trimer and E-domain dimer). Mutant structures were generated by MD simulation using WT structures as templates. Figures for protein structures were created using VMD software (Humphrey et al., 1996).

Molecular Dynamic (MD) Simulations and Thermodynamic Integration (TI). MD simulations were preformed using PMEMD.CUDA (Salomon-Ferrer et al., 2013) in the AMBER18 package (D.A. Case, 2018) with the ff14SB force field (Maier et al., 2015). Gephyrin G-domain trimers and E-domain dimers were explicitly solvated with TIP3P water molecules (Jorgensen et al., 1983) in a rectangular box; a distance of 12 Å from the protein to the edge of the solvent box was chosen, and periodic boundary conditions were applied. Sodium ions were added to neutralize the system. The WT consisted of 85,173 atoms in the G-domain trimer and 104,523 atoms in the E-domain dimer. The particle-mesh Ewald (PME) method was applied for treatment of long-range electrostatic interactions, and a 9.0 Å force-shifted cutoff was used for short-range non-bonded interactions. The equilibrium bond length of hydrogen atoms was constrained using the SHAKE algorithm (Ryckaert et al., 1977); 2,500 steps of steepest decent minimization followed by 2,500 steps for conjugate gradient minimization were

performed. The systems were subsequently subjected to a 25-ps heating process in which the temperature was raised gradually from 10 K to 298 K with an NVT ensemble. After heating, a 25-ps equilibrium process using an NPT ensemble was applied. Production runs were carried out for 1 μs, with a 2 fs time step and applying the NPT ensemble. Temperature and pressure were controlled with a Langevin dynamic thermostat using a collision frequency of 1 ps−1 and a weak-coupling barostat with a coupling constant of 0.5 ps. All trajectories were recorded every 10 ps intervals. Each system was simulated for 5 independent trajectories, and a total of 40 trajectories were produced. The trajectories were analyzed using CPPTRAJ tools in the AmberTools package (D.A. Case, 2018). The backbone RMSF (root-mean-square-fluctuation) was calculated for backbone atoms (N, Cα, C) of gephyrin residues in 0.5~1 μs time windows of trajectories using the 'atomicfluc' command with the 'byres' option in CPPTRAJ (**Fig. S1**). TI-MD simulations were performed using the AMBER18 package with ff14SB force field (Lee et al., 2017; Mermelstein et al., 2018), and binding free energy differences were calculated using a thermodynamic cycle in conjunction with the condition of equal energy differences (**Fig. S6**). ΔG1 (ΔG2) is defined as the binding free energy between monomeric and multimeric states of the WT or mutant; ΔG3 (ΔG4) is the free energy difference between WT and mutant monomers (multimer). The thermodynamic equality is ΔG1+ΔG4-ΔG2-ΔG3 = 0. To obtain the binding free energy differences between WT and mutants, we can arrange the equation for the thermodynamic cycle as ΔG2-ΔG1 = ΔG4-ΔG3 = ΔΔG. The TI method, which uses a mixed potential function, was applied for calculating ΔG3 and ΔG4, and softcore potentials were used for smoothing the appearance and disappearance of atoms in van der Waals and electrostatic interactions in the hybrid state. In the TI calculation, the following Hamiltonian was used:

$$H_{\lambda} = (1-\lambda)H_{\mathrm{WT}} + \lambda H_{\mathrm{mutant}}$$

where λ is the weight of the mutant state and varies from 0 to 1. For example, if λ is 0.4, the mixed state has 60% WT structure and 40% mutant structure at the same position. As a result, the final structure of the hybrid state has mixed potential. The equations for vdW and electrostatic potential in softcore as follows:

$$V^{\text{vdW}}_{\text{WT,disappearing}} = 4\varepsilon(1-\lambda)\left[\frac{1}{\left[a\lambda+\left(\frac{r_{ij}}{\sigma}\right)^6\right]^2}-\frac{1}{a\lambda+\left(\frac{r_{ij}}{\sigma}\right)^6}\right]$$

$$V^{\text{vdW}}_{\text{mutant,appearing}} = 4\varepsilon\lambda\left[\frac{1}{\left[a(1-\lambda)+\left(\frac{r_{ij}}{\sigma}\right)^6\right]^2}-\frac{1}{a(1-\lambda)+\left(\frac{r_{ij}}{\sigma}\right)^6}\right]$$

$$V^{\text{elec}}_{\text{WT,disappearing}} = (1-\lambda)\frac{q_i q_j}{4\pi\varepsilon\sqrt{\beta\lambda+r_{ij}^2}}$$

$$V^{\text{elec}}_{\text{mutant,appearing}} = \lambda\frac{q_i q_j}{4\pi\varepsilon\sqrt{\beta(1-\lambda)+r_{ij}^2}}$$

We constructed the coordinate and parameter files for the hybrid state using the 'tleap' program. We also modified parameter files for mutation points at each chain using the 'parmed' module in AMBER. The major input file options for AMBER TI calculations are icfe = 1 (free energy calculation), ifsc =1 (softcore potential), scalpha = 0.5 (softcore potential parameter α), scbeta = 12.0 (softcore potential parameter β), temp0 = 300 (temperature, K) and clambda (λ). The free energy difference (ΔG) was calculated using Gaussian quadrature according to following formula:

$$\Delta G = \int_0^1 \langle\frac{\partial v}{\partial\lambda}\rangle_\lambda \approx \sum_i w_i \langle\frac{\partial v}{\partial\lambda}\rangle_i$$

We used a 9-point quadrature, with λ set to 0.01592, 0.08198, 0.19331, 0.33787, 0.5, 0.66213, 0.80669, 0.91802 and 0.98408, and weights of 0.04064, 0.09032, 0.13031, 0.15617, 0.16512, 0.15617, 0.13031, 0.09032 and 0.04064, respectively. A 5-ns TI simulation was performed for each λ value and 5 ensembles for each system. The binding free energy differences (ΔΔG) were applied cumulative average over course of the simulation and averaged for 5 trajectories of each gephyrin mutant.

Construction of Expression Vectors. ***1. Gephyrin***. pEGFP-Gephyrin wild-type (WT) was previously described (Papadopoulos et al., 2017). EGFP-Gephyrin A91T and pEGFP-Gephyrin G375D mutants were generated with a site-directed mutagenesis kit (Stratagene) using pEGFP-Gephyrin WT as a template. AAVs encoding full-length gephyrin WT, A91T or G375D were generated by PCR amplification of the corresponding pEGFP-gephyrin constructs and subsequent subcloning into *Xba*I and *BamH*I sites of the pAAV-T2A-EGFP vector (Kim et al., 2020). Gephyrin WT was generated by PCR amplification of the full-length region and subsequent subcloning into the L-313 vector at *EcoR*I and *BamH*I sites. pL313-Gephyrin A91T and G375D were generated with a site-directed mutagenesis kit (Stratagene) using pL313-Gephyrin WT as a template. ***2. Others***. The plasmids pAAV-hSyn-ΔCre-mCherry and pAAV-hSyn-Cre-mCherry were kindly provided by Dr. Thomas C. Südhof (Stanford University, Palo Alto, CA, USA).

Antibodies. The following commercially available antibodies were used: goat polyclonal anti-EGFP (Rockland), rabbit polyclonal anti-$GABA_AR\gamma2$ (Synaptic Systems), rabbit polyclonal anti-Nlgn2 (Synaptic Systems), rabbit polyclonal anti-Collybistin (Synaptic Systems), mouse monoclonal anti-Gephyrin (clone 3B11; Synaptic Systems), rabbit polyclonal anti-VGAT (Synaptic Systems), mouse monoclonal anti-VGAT (Synaptic Systems), rabbit monoclonal anti-TrkC (C44H4; Cell Signaling), rabbit polyclonal anti-PSD-95 (JK016; Um et al., 2016) and rabbit polyclonal anti-IQSEC3 (JK079; (Kim et al., 2020)).

Gel Filtration Chromatography. HEK293T cells transfected with the indicated gephyrin expression vectors were harvested in phosphate-buffered saline (PBS), washed once with PBS, homogenized with an ultrasonicator in 1 ml of buffer A (50 mM Tris-HCl, pH 7.5; 150 mM NaCl; 5 mM DTT), and centrifuged at 10,000 × g for 15 minutes. The resulting supernatant was applied to a Superdex 200 10/300 GL column attached to an AKTA Purifier FPLC (GE Healthcare) and eluted with PBS containing 0.2 μm filtered 0.05% bovine serum albumen (BSA) at a flow rate of 0.5 ml/min. Aliquots (100 μl) of each fraction were collected and immunoblotted using anti-gephyrin antibodies. Globular protein size

standards (Sigma), including thyroglobulin (670 kDa), apoferritin (480 kDa), β-Amylase (223.8 kDa), alcohol dehydrogenase (141 kDa), bovine serum albumin (66 kDa), and ovalbumin (43 kDa) were run in parallel under identical experimental settings.

Neuron Culture, Transfections, Imaging, and Quantitation. Cultured hippocampal neurons were prepared from E18 rat brainscultured on coverslips coated with poly-L-lysine, and grown in Neurobasal medium supplemented with B-27 (Invitrogen), 0.5% FBS, 0.5 mM GlutaMax (Invitrogen), and sodium pyruvate (Invitrogen). For overexpression of gephyrin in cultured neurons, hippocampal neurons were transfected with pEGFP-Gephyrin WT or the indicated point mutants, or with EGFP (Control) using CalPhos Kit (Clontech) at DIV10 and immunostained at DIV14. For immunocytochemistry, cultured neurons were fixed with 4% paraformaldehyde/4% sucrose, permeabilized with 0.2% Triton X-100 in PBS, immunostained with primary antibodies as indicated, and detected with Cy3- and fluorescein isothiocyanate (FITC)-conjugated secondary antibodies (Jackson ImmunoResearch). Images were acquired using a confocal microscope (LSM800, Carl Zeiss) with a 63 x objective lenses; all image setting were kept constant. Z-stack images were converted to maximal projection and analyzed to obtain the size, intensity, and density of puncta immunoreactivities of marker proteins. Quantification was performed in a blinded manner using MetaMorph software (Molecular Devices). For quantification of GABAergic synaptic targeting of EGFP-gephyrin, overlaying red ($GABA_AR\gamma2$) and magenta (VGAT) color images were obtained using the color threshold function in ImageJ. Regions of interests (ROIs) from distal dendrites were defined according to pEGFP-signals. The degree of colocalization of green (pEGFP-gephyrin) and overlaid red ($GABA_AR\gamma2$) and magenta (VGAT) in the ROIs was calculated using the colocalization function in MetaMorph. The value for WT gephyrin was normalized to 1.

Production of Recombinant Adeno-associated Viruses (AAVs). Recombinant AAVs were packaged with high efficiency using pHelper and AAV1.0 (serotype 2/9) capsids. HEK293T cells were cotransfected with pHelper and pAAV1.0, together with pAAV-hSyn-ΔCre-EGFP, pAAV-hSyn-Cre-EGFP, pAAV-hSyn-ΔCre-mCherry, pAAV-hSyn-Cre-mCherry, pAAV-Gephyrin WT-T2A-GFP, pAAV-

Gephyrin A91T-T2A-EGFP, or pAAV-Gephyrin G375D-T2A-EGFP. Transfected HEK293T cells were harvested 72–108 hours post transfection. After addition of 0.5 M EDTA to the medium, cells were washed three times with PBS and collected by centrifugation. Cells were then resuspended in PBS and lysed by subjecting to four freeze-thaw cycles in an ethanol/dry ice bath (7 minutes each) and 37°C water bath (5 minutes). Lysates were centrifuged, and supernatants were collected and incubated with a solution containing 40% poly(ethylene glycol) (Sigma) and 2.5 M NaCl on ice for 1 hour and centrifuged at 2000 rcf for 30 minutes. The pellets were resuspended in HEPES buffer (20 mM HEPES pH 8.0, 115 mM NaCl, 1.2 mM $CaCl_2$, 1.2 mM $MgCl_2$, 2.4 mM KH_2PO_4), mixed with chloroform, and centrifuged at 400 rcf for 10 minutes. The supernatant was collected and concentrated using Amicon Ultra Centrifugal Filters (0.5 ml, 3K MWCO; Millipore). Viruses were assessed for infectious titer by RT-PCR, and used for infections at 10^{10}–10^{12} infectious units/μl.

Stereotactic Surgery. For stereotaxic delivery of recombinant AAVs, 6–week-old gephyrin floxed mice were anesthetized by inhalation of isoflurane (3–4%) or intraperitoneal injection of 2% 2,2,2-tribromoethanol (Sigma) in saline, and secured in a stereotaxic apparatus. Viral solutions were injected with a Hamilton syringe using a Nanoliter 2010 Injector (World Precision Instruments) at a flow rate of 50 nl/min (injected volume, 0.3 μl). The coordinates used for stereotaxic injections into the hippocampal DG of mice were as follows: anteroposterior (AP), -2.1 mm; medial–lateral (ML), ± 1.2 mm; and dorsal–ventral (DV), 2.2 mm from bregma. Each injected mouse was returned to its home cage and used for scoring seizure-like behaviors, immunohistochemical analyses, or electrophysiological recordings after 2 weeks.

***In Vivo* Coimmunoprecipitation Assays.** Brains from 6–week-old gephyrin floxed mice expressing pAAV-Cre or pAAV-Cre together with pAAV-Gephyrin WT, A91T or G375D (delivered by stereotactic injection) were homogenized in 10 ml of ice-cold homogenization buffer consisting of 320 mM sucrose, 5 mM HEPES-NaOH (pH 7.5), 1 mM EDTA, 0.2 mM PMSF, 1 μg/ml aprotinin, 1 μg/ml leupeptin, 1 μg/ml pepstatin, and 1 mM Na_3VO_4. The homogenized tissue was centrifuged at $1000 \times g$ for 10

minutes, after which the supernatant was centrifuged at 15,000 × g for 20 minutes. The pellets were homogenized in buffer consisting of 20 mM HEPES-NaOH (pH 7.5), 0.15 M NaCl, 2 mM $CaCl_2$, 2 mM $MgCl_2$, 0.2 mM PMSF, 1 μg/ml aprotinin, 1 μg/ml leupeptin, 1 μg/ml pepstatin, and 1 mM Na_3VO_4. Triton X-100 was added to a final concentration of 1% (w/v) and dissolved with constant stirring at 4°C for 1 hour. Supernatants obtained after centrifugation at 15,000 × g for 20 minutes were incubated with anti-gephyrin or anti-$GABA_AR\gamma2$ antibody overnight at 4°C, followed by addition of 30 μl of a 1:1 suspension of protein G-Sepharose (Incospharm Corporation), after which the mixture was incubated for 2 hours at 4°C with gentle rotation. The beads were pelleted and washed three times with lysis buffer (20 mM HEPES-NaOH pH 7.5, 0.15 M NaCl, 2 mM $CaCl_2$, 2 mM $MgCl_2$, 0.2 mM PMSF, 1 μg/ml aprotinin, 1 μg/ml leupeptin, 1 μg/ml pepstatin, and 1 mM Na_3VO_4). Immune complexes were then resolved by SDS-PAGE and immunoblotted with anti-gephyrin, anti-Nlgn2, anti-Collybistin, anti-IQSEC3, anti-PSD-95, anti-TrkC and anti-$GABA_AR\gamma2$ antibodies, each at a concentration of 1 μg/ml.

Immunohistochemistry. Six–week-old male C57BL/6N mice stereotactically injected with the indicated AAVs were anesthetized and immediately perfused, first with PBS for 3 minutes and then with 4% paraformaldehyde for 5 minutes. Brains were dissected out, fixed overnight in 4% paraformaldehyde, incubated overnight with 30% sucrose (in PBS), and then sliced into 30-μm-thick coronal sections using a vibratome (Model VT1200S; Leica Biosystems). Sections were permeabilized by incubating with 1% Triton X-100 in PBS containing 5% BSA and 5% horse serum for 30 minutes. For immunostaining, sections were incubated for 8–12 hours at 4 °C with primary antibodies in the same blocking solution. Sections were washed three times in PBS and incubated with the appropriate Cy3-, fluorescein isothiocyanate (FITC)-conjugated secondary antibodies (Jackson ImmunoResearch) or Alexa Fluor® 647-conjugated secondary antibodies (ThermoFisher Scientific) for 2 hours at room temperature. After three washes with PBS, sections were counterstained with DAPI (4',6-diamidino-2-phenylinodole) and mounted onto glass slides (Superfrost Plus; Fisher Scientific) with VECTASHIELD mounting medium (H-1200; Vector Laboratories).

Seizure Behavior Scoring. Six-week-old male C57BL/6N mice stereotactically injected with the indicated AAVs were administered KA (15 mg/kg; Sigma Cat. No. K0250) or saline (control), and the resulting seizure behaviors were video-recorded for the next 2 hours. Seizure susceptibility was measured by rating seizures every 3 minutes on a scale of 0 to 5, as follows: 0, no abnormal behavior; 1, reduced motility and prostate position; 2, partial clonus; 3, generalized clonus including extremities; 4, tonic-clonic seizure with rigid paw extension; and 5, death.

Electroencephalography (EEG) Recordings and Analyses. For EEG recordings, 6–week-old male C57BL/6N mice stereotactically injected with the indicated AAVs were anesthetized with isoflurane (3-4%) and secured in a stereotaxic apparatus to prevent limb-withdrawal response to a noxious foot pinch. After injection of the indicated concentrated AAVs into the hippocampal DG of experimental mice prabove, four additional holes were drilled in the skull without puncturing the meninges, and electrodes were carefully attached with prefabricated headmounts and secured with dental acrylic. Recording electrodes were placed in the parietal lobe (AP -2.4 mm; ML ± 1.4 mm), and reference electrodes were placed in the occipital lobe. The LFP electrode was inserted at the DG (AP -2.4 mm; ML ± 1.3 mm, DV -2.2). After a 2-week recovery period, mice connected to the EEG/EMG three-channel monitoring system, composed of preamplifier and a commutator for data acquisition (Pinnacle Technology) with time-lock video recording, were transferred to an acrylic cage (25 × 25 × 45 cm). Each mouse was subjected to a 24-hour recording session for measuring spontaneous seizures and a 4-hour recording session for measuring KA-induced seizures. Data were recorded at a sampling rate of 2000 Hz, with application of a 100-Hz loss-pass filter. Off-line EEG analyses were performed manually in MatLab (Mathworks) using EEGlab (SCCN)) or LabChart 8.0 software (ADInstruments). For manual analyses of electrographic seizures, the following previously described criteria were used, with minor modifications (Baraban et al., 2009): grade I, basic background, no epileptiform spikes; grade II, mostly normal background, some high-voltage spikes; grade III, mostly abnormal background with low-frequency, high-voltage spiking; and grade IV, high-frequency, high-voltage, synchronized polyspike waves with amplitudes > 3-fold baseline. Only ictal seizures (grade III or IV) lasting longer than 3

seconds were included in the analysis. For automated quantification of interictal spikes, selected frequencies (0–60 Hz) were digitally filtered using low-pass filter in LabChart 8.0 software (ADInstruments), and amplitudes > 3-fold baseline discharges were automatically calculated using the native LabChart function.

QUANTIFICATION AND STATISTICAL ANALYSIS

Data Analysis and Statistics. All data are expressed as means ± SEM. All experiments were repeated using at least three independent cultures, and data were statistically evaluated using a Mann-Whitney *U* test, Kruskal-Wallis test (one-way ANOVA on ranks) followed by Dunn's pairwise *post hoc* test, as appropriate. Prism7.0 (GraphPad Software) was used for analysis of data and preparation of bar graphs. P-values < 0.05 were considered statistically significant (individual *p*-values are presented in figure legends).

SUPPLEMENTAL REFERENCES

D.A. Case, I.Y.B.-S., S.R. Brozell, D.S. Cerutti, T.E. Cheatham, III, V.W.D. Cruzeiro, T.A. Darden, R.E. Duke, D. Ghoreishi, M.K. Gilson, H. Gohlke, A.W. Goetz, D. Greene, R Harris, N. Homeyer, S. Izadi, A. Kovalenko, T. Kurtzman, T.S. Lee, S. LeGrand, P. Li, C. Lin, J. Liu, T. Luchko, R. Luo, D.J. Mermelstein, K.M. Merz, Y. Miao, G. Monard, C. Nguyen, H. Nguyen, I. Omelyan, A. Onufriev, F. Pan, R. Qi, D.R. Roe, A. Roitberg, C. Sagui, S. Schott-Verdugo, J. Shen, C.L. Simmerling, J. Smith, R. Salomon-Ferrer, J. Swails, R.C. Walker, J. Wang, H. Wei, R.M. Wolf, X. Wu, L. Xiao, D.M. York and P.A. Kollman (2018). AMBER 2018. University of California, San Francisco.

Humphrey, W., Dalke, A., and Schulten, K. (1996). VMD: visual molecular dynamics. J Mol Graph 14, 33-38, 27-38.

Jorgensen, W.L., Chandrasekhar, J., Madura, J.D., Impey, R.W., and Klein, M.L. (1983). Comparison of simple potential functions for simulating liquid water. J Chem Phys 79, 926-935.

Kim, S., Kim, H., Park, D., Kim, J., Hong, J., Kim, J.S., Jung, H., Kim, D., Cheong, E., Ko, J., et al. (2020). Loss of IQSEC3 Disrupts GABAergic Synapse Maintenance and Decreases Somatostatin Expression in the Hippocampus. Cell Reports 30.

Lee, T.S., Hu, Y., Sherborne, B., Guo, Z., York, D.M. (2017). Toward fast and accurate binding affinity prediction with pmemdGTI: an efficient implementation of GPU-accelerated thermodynamic integration. J Chem Theor Comput 13, 3077-3084

Maier, J.A., Martinez, C., Kasavajhala, K., Wickstrom, L., Hauser, K.E., and Simmerling, C. (2015). ff14SB: Improving the Accuracy of Protein Side Chain and Backbone Parameters from ff99SB. J Chem Theory Comput 11, 3696-3713.

Maric, H.M., Kasaragod, V.B., Hausrat, T.J., Kneussel, M., Tretter, V., Stromgaard, K., and Schindelin, H. (2014). Molecular basis of the alternative recruitment of GABA(A) versus glycine receptors through gephyrin. Nat Commun 5, 5767.

Mermelstein, D.J., Lin, C., Nelson, G., Kretsch, R., McCammon, J.A., Walker, R.C. (2018). Fast and flexible gpu accelerated binding free energy calculations within the amber molecular dynamics package. J Comput Chem 39, 1354-1358.

O'Sullivan, G.A., Jedlicka, P., Chen, H.X., Kalbouneh, H., Ippolito, A., Deller, T., Nawrotzki, R.A., Kuhse, J., Kalaidzidis, Y.L., Kirsch, J., et al. (2016). Forebrain-specific loss of synaptic GABAA receptors results in altered neuronal excitability and synaptic plasticity in mice. Mol Cell Neurosci 72, 101-113.

Papadopoulos, T., Rhee, H.J., Subramanian, D., Paraskevopoulou, F., Mueller, R., Schultz, C., Brose, N., Rhee, J.S., and Betz, H. (2017). Endosomal Phosphatidylinositol 3-Phosphate Promotes Gephyrin Clustering and GABAergic Neurotransmission at Inhibitory Postsynapses. J Biol Chem 292, 1160-1177.

Ryckaert, J.-P., Ciccotti, G., and Berendsen, H.J.C. (1977). Numerical integration of the cartesian equations of motion of a system with constraints: molecular dynamics of n-alkanes. Journal of Computational Physics 23, 327-341.

Salomon-Ferrer, R., Gotz, A.W., Poole, D., Le Grand, S., and Walker, R.C. (2013). Routine Microsecond Molecular Dynamics Simulations with AMBER on GPUs. 2. Explicit Solvent Particle Mesh Ewald. J Chem Theory Comput 9, 3878-3888.

Sola, M., Kneussel, M., Heck, I.S., Betz, H., and Weissenhorn, W. (2001). X-ray crystal structure of the trimeric N-terminal domain of gephyrin. J Biol Chem 276, 25294-25301.

Schwarz, G., Schrader, N., Mendel, R.R., Hecht, H.J., and Schindelin, H. (2001). Crystal structures of human gephyrin and plant Cnx1 G domains: comparative analysis and functional implications. J Mol Biol 312, 405-418.

Um, J.W., Choi, T.Y., Kang, H., Cho, Y.S., Choii, G., Uvarov, P., Park, D., Jeong, D., Jeon, S., Lee, D., et al. (2016a). LRRTM3 Regulates Excitatory Synapse Development through Alternative Splicing and Neurexin Binding. Cell Rep 14, 808-822.

Webb, B., and Sali, A. (2016). Comparative Protein Structure Modeling Using MODELLER. Curr Protoc Protein Sci 86, 2 9 1-2 9 37.